Materials Characterization 159 (2020) 110046

Contents lists available at ScienceDirect

Materials Characterization

journal homepage: www.elsevier.com/locate/matchar

High-strength $Al_{0.2}Co_{1.5}CrFeNi_{1.5}Ti$ high-entropy alloy produced by powder metallurgy and casting: A comparison of microstructures, mechanical and tribological properties

Larissa Moravcikova-Gouvea[a,*], Igor Moravcik[a], Milan Omasta[b], Jozef Veselý[c], Jan Cizek[a,d], Peter Minárik[c], Jan Cupera[a], Antonín Záděra[b], Vit Jan[a], Ivo Dlouhy[a]

[a] Institute of Materials Science and Engineering, Brno University of Technology, Technicka 2896/2, 616 69 Brno, Czech Republic
[b] Faculty of Mechanical Engineering, Brno University of Technology, Technicka 2896/2, 616 69 Brno, Czech Republic
[c] Charles University, Faculty of Mathematics and Physics, Department of Physics of Materials, Ke Karlovu 5, Praha 2, 121 16, Czech Republic
[d] Institute of Plasma Physics, The Czech Academy of Sciences, Za Slovankou 1782/3, 182 00, Prague 8, Czech Republic

ARTICLE INFO

Keywords:
High–entropy alloys
Microstructure
Mechanical properties
Tribological properties
Powder metallurgy
Casting

ABSTRACT

This work presents an in-depth comparison of the microstructural origins of high strength and high wear resistance in the $Al_{0.2}Co_{1.5}CrFeNi_{1.5}Ti$ high-entropy alloy produced by powder metallurgy (PM) and casting.

The PM alloy microstructure is composed almost exclusively of fine-grained FCC phase with minor, in-situ formed TiC particles. The latter is responsible for a grain-boundary pinning effect and, consequently, the high-hardness of 712 HV was achieved allied with excellent flexural strength (2018 MPa) and elastic modulus of 258 GPa. Its wear properties surpass those of the wear-resistant AISI 52100 steel under 1.2 N load. Despite the high strength properties of PM alloy, a ductile fracture behaviour was retained.

In contrast, the cast alloy is composed of a coarse-grained dendritic microstructure of FCC matrix containing a complex of intermetallic phases. Its tribological properties are superior to traditional AISI 52100 steel under all sliding conditions, exhibiting the best results among all tested materials. However, its elastic modulus (210 GPa) and flexural strength (1101 MPa), at a comparable hardness level (682 HV), were significantly lower when compared to the PM counterpart. This stems from the intrinsic brittleness of the cast material, a consequence of its complex microstructure, exhibiting pure cleavage-type fracture in several areas of the fracture surface.

1. Introduction

High-entropy alloys (HEAs), also known as multi-principal element alloys, have attracted significant interest in the materials science community in the past few years [1–3] due to their distinctive properties resulting from the novelty of their design concept. HEAs comprise at least five elements with near equiatomic compositions without a prominent base element, distinguishing them from the conventional alloying approach, which typically involves a single-base element with the addition of small proportions of other constituents [4–6].

The metallurgical approach to HEA design is to stabilize the disordered phase, thereby suppressing the formation of ordered intermetallics by maximizing the configurational entropy. Indeed, this strategy has been shown to produce stable single-phase solid solution face-centered-cubic (FCC) and body-centered-cubic (BCC) alloys [7–9]. However, the majority of HEAs studied so far have been proven to form intermetallic phases in specific conditions. These include the cases when the alloy contains elements with great differences in atomic radius and large negative enthalpies of mixing [8,10–12].

To date, HEAs have demonstrated promising potential for industrial applications due to some of their unique properties, such as an interesting combination of high strength and good ductility [13–16], even at cryogenic temperatures [17], as well as high-temperature strength [18,19], high wear resistance [20], high thermal stability [21,22], good corrosion resistance [23], etc.

Among the superior wear-resistant HEAs, the AlCoCrFeNiTi composition and its variants—particularly $Al_{0.2}Co_{1.5}CrFeNi_{1.5}Ti$—emerge as interesting choices, as they have been reported to possess excellent wear properties allied with high hardness [20,24].

HEAs are generally fabricated by casting. Nonetheless, casting is subject to processing problems that may be detrimental for the final material. Since the alloys comprise multiple elements, they may suffer

---

[*] Corresponding author.
E-mail address: gouvea@fme.vutbr.cz (L. Moravcikova-Gouvea).

https://doi.org/10.1016/j.matchar.2019.110046
Received 17 September 2019; Received in revised form 27 November 2019; Accepted 27 November 2019

from selective evaporation of elements with intrinsic low-melting temperatures or segregation of elements with high-melting points during the melting. Furthermore, as-cast HEAs usually possess coarse dendritic structures with precipitation of brittle intermetallic phases [1,10,25].

Alternatively, powder metallurgy (PM) has been proven to be a reliable and low-cost method capable of relatively easy and efficient production of a varied range of advanced materials, including HEAs [26–29]. Compared to casting, PM requires lower temperatures for processing since it can be realized through solid-state sintering.

The selection of the processing methods is a critical factor influencing the microstructure, phase formation and its kinetics, as well as mechanical and tribological properties of any material. That said, the final properties and, therefore, suitability to different applications can be greatly affected and may be tailored by fine-tuning of a selected production technique.

Somewhat surprisingly, to the best of our knowledge, for HEAs, only a single study comparing the consequences of the selection of the manufacturing routes has been reported so far [28], where the differences in mechanical behaviour and strengthening mechanisms of a HEA are described.

In this light, this work presents a unique comparison of the $Al_{0.2}Co_{1.5}CrFeNi_{1.5}Ti$ produced by two different manufacturing routes, powder metallurgy and casting. A comprehensive evaluation of the influence of the two processing methods on the alloy's bending strength, wear-resistance and hardness were performed for the first time in a single study using identical experimental conditions, supported by an extensive microstructural characterization to understand the phenomena underlying the mechanical and tribological behaviours. The microstructures were characterized by a combination of X-ray diffraction (XRD), transmission electron microscopy (TEM), and electron backscattered diffraction (EBSD) supported by phase predictions using the CALPHAD approach.

2. Materials and methods

2.1. Preparation of samples

The PM alloy was prepared by high-energy ball milling of feedstock powders and subsequent spark plasma sintering. Elemental powders of Al, Co, Cr, Fe, Ni and Ti (99.5 wt% purity, Sigma Aldrich) mixed in $Al_{0.2}Co_{1.5}CrFeNi_{1.5}Ti$ stoichiometric ratio were processed by mechanical alloying in a Fritsch Pulverisette 6 planetary ball mill. The milling was carried out under high-purity nitrogen atmosphere (99.9999%) in a sealed bowl, containing hardened bearing steel balls (AISI 52100 – SUJ2) of 15 mm diameter in a 10:1 ball-to-powder weight ratio (BPR). The milling was conducted with a milling speed of 300 RPM for a total 5 h, comprising of five cycles of 60 min of milling and 30 min idle time. Wet milling in toluene for additional 30 min was necessary in order to remove the powder stuck to the milling balls surfaces.

The milled powders were then consolidated by spark plasma sintering technology (Thermal Technology LLC 10-4, USA) using a graphite die with an inner diameter of 30 mm, in vacuum atmosphere at a constant pressure of 30 MPa. The following densification scheme was used: 100 $^\circ C\cdot min^{-1}$ heating rate from RT up to 1000 °C with a 15 min dwell time at 550 °C to remove any organic compounds potentially present. Subsequently, 50 $^\circ C\cdot min^{-1}$ rate was used from 1000 °C up to 1100 °C with the final 10 min dwell time at 1100 °C. After densification, the electric current of the SPS machine was turned off and the sample was spontaneously cooled down to room temperature in a fast rate.

In order to compare the effect of different manufacturing routes in terms of microstructural, chemical and mechanical features of both materials, the $Al_{0.2}Co_{1.5}CrFeNi_{1.5}Ti$ alloy was also prepared by vacuum induction melting from elemental constituents with purities higher than 99.5 wt%. The ingot was cast under argon atmosphere.

From the bulk materials, samples for microstructural observations were prepared by hot mounting in polymeric resin and mechanically ground with SiC abrasive papers down to #2400 grit. The samples were then polished using 3 μm and 1 μm diamond paste. The last step of sample preparation was mechano-chemical polishing using Struers OPS suspension.

The samples for flexural strength determination had dimensions of $3 \times 4 \times 18\ mm^3$ and were manufactured by electric discharge machining (EDM). To decrease the influence of surface roughness on the measured values, the samples were polished to mirror finish. The $4 \times 18\ mm^2$ face of these samples corresponded to the direction perpendicular to the SPS pressing direction for PM HEA.

For wear testing, samples of both PM and Cast HEA were machined to dimensions of $5 \times 5 \times 28\ mm^3$ and successively ground with #250-2000 grit SiC papers, followed by polishing with 3 mm and 1 mm diamond paste using a linen disc.

2.2. Microstructural and chemical characterization

X-ray diffraction analysis (XRD) of the materials phase composition was carried out using Philips X'Pert Pro diffractometer operated at 40 kV voltage with the current of 30 mA. A continuous scanning was performed with 2θ between 30° and 100° using a speed of $0.02^\circ\cdot min^{-1}$ and a step size of 0.0167°. The radiation used was Cu-Kα with $\lambda = 1.54056$ Å.

Thin foil specimens were prepared for TEM (Jeol 2200FS) observation of the microstructure by Focused Ion Beam (FIB) micromachining inside ZEISS Auriga SEM chamber.

The scanning electron microscope (SEM) characterization of the materials was performed using ZEISS Ultra Plus FEG microscope in secondary (SE) and backscattered electrons (BSE) modes. Electron backscattered diffraction (EBSD) mapping and energy-dispersive X-ray analysis (EDS) were used for the evaluation of grain structure/lattices and chemical composition, respectively. For EBSD measurements, the reference direction for inverse pole figures (IPF) was perpendicular to the SPS pressing direction as a texture was most likely to be formed along this direction. The presented values of grain sizes and volume fractions of respective phases have been calculated as an average of measurements from three randomly selected areas. Image J software (NIH, USA) has been used for residual porosity calculation from the obtained images.

Calculation of phase diagrams (CALPHAD) were performed using ThermoCalc software version 2019a (TCHEA3 database version 3.1).

2.3. Mechanical and tribological properties characterization

Vickers hardness measurements were carried out following ISO 6507 standard using LM 247AT microhardness tester under the load of 0.2 kg and dwell time of 10 s. The individual results for the materials in their as-produced states represent an average of at least 15 measurements and the error is the standard deviation. For the materials after tribological tests, hardness measurements were taken using Vickers indenter with 0.2 kg load, on the same surface of the test in a perpendicular direction to the worn track. The results for each material are taken from at least five perpendicular lines to the track containing 15 measurements and the error is the standard deviation.

Nanoindentation testing was performed in order to calculate the elastic modulus of the materials according to Oliver & Pharr method [30]. CSM Instruments NHT2 nanoindentation tester equipped with a Berkovich diamond indenter was used at acquisition rate of 10 Hz, maximum load of 100 mN, loading and unloading rates of 200 $mN\cdot min^{-1}$, and dwell time of 10 s. Averages taken from at least 30 indents for each sample are presented, where the error is the standard deviation of the measurements.

Flexural strength (R_{mo}) determination was performed using three-point bending jig of Zwick Z020 universal tensile test machine, with the loading span of 18 mm and a crosshead speed of 1 $mm\cdot min^{-1}$. Four specimens were used for each material and the results were taken as an average of the measurements. The calculated error represents the standard deviation.

The wear testing was done on the commercial UMT TriboLab tribometer using the reciprocal ball-on-plate scheme. During testing, the samples performed a reciprocating movement under dry sliding conditions, while a 9.51 mm-diameter bearing steel (AISI 52100 – SUJ2) counterpart ball was fixed stationary on the top of the plate under an applied normal load. As a reference material, a high-speed bearing steel (AISI 52100 – SUJ2) bar was chosen due to its exceptional mechanical properties in terms of wear, and also to facilitate a direct comparison with a previous study on cast high-entropy alloys [20]. As a second reference material, as-cast Inconel 713 was used due to its crystallographic similarity to the presented PM-HEA alloy (FCC matrix with dispersed coherent precipitates). The reference materials and the HEAs were tested under identical conditions.

The used parameters of the wear testing were normal loads of 1.2 N and 5 N, stroke length of 10 mm, stroke frequency of 2 Hz and test duration of 30 min (corresponding to a total sliding distance of 36 m). The friction force was monitored and recorded in-situ, while the specific wear rates of the studied materials were quantified according to the Archard's model equation [31]:

$$(\mathit{Specific\ wear\ rate}) = \frac{\mathit{wear\ volume}}{\mathit{load} * \mathit{distance}}, \tag{1}$$

where the wear volume was calculated as the product of the worn cross-sectional area measured with the optical profilometer Contour GT, and the total sliding distance.

The maximum contact pressure p_{max} under the selected load was calculated according to the Hertzian contact stress theory for spheres in contact with flat surface, which gives a description of the stress within mating parts following the model's equation [32]:

$$p_{max} = \frac{1}{\pi}\left(\frac{6FE^{*2}}{R^2}\right)^{1/3}, \tag{2}$$

where F is the applied normal force, R is the radius of the sphere and E^* relates the elastic moduli of the ball (E_1) and the tested materials (E_2) and its respective Poisson ratios (ϑ_1, ϑ_2) according to:

$$\frac{1}{E^*} = \frac{1-\vartheta_1^2}{E_1} + \frac{1-\vartheta_2^2}{E_2}. \tag{3}$$

The corresponding coefficients of friction (COF) were calculated as a ratio between the applied normal and friction forces and their respective errors are the standard deviation of the measurement.

3. Results and discussion

3.1. Phase prediction – CALPHAD

To discuss the experimental findings of this study, thermodynamic calculation of phase diagrams (CALPHAD) for $Al_{0.2}Co_{1.5}CrFeNi_{1.5}Ti$ (stoichiometric ratio) high-entropy alloy were computed. The diagram is shown in Fig. 1a. The alloy designed in this study possesses 3.2 at.% Al (denoted by the red arrow in Fig. 1a).

Due to the large negative enthalpy of mixing for Al-containing HEAs, intermetallics are more likely to be formed, leading to a multiphase structure in which the relative volumes of FCC and BCC phases are strongly dependent on the cooling rates [33]. The high molar ratios of Co and Ni, known as being efficient FCC formers, guarantee that FCC remains the dominant phase. The FCC matrix renders more workability to the alloy, while, at the same time, the presence of intermetallics ensures preserving a high strength in the material. This can be further improved by precipitation hardening, a process used in some Ni-base superalloys [34].

For this alloy, the predicted melting temperature is approximately 1150 °C. Between temperatures (T) 1150 °C and approximately 1135 °C, nucleation of the B2 phase should occur. For temperatures (T) between 1135 °C $< T <$ 1125 °C, nucleation of the FCC phase starts. For the temperature range 1125 °C $< T <$ 800 °C, concurrent nucleation and growth of BCC, FCC and $L1_2$ should take place. Further temperature reduction induces the subsequent formation of sigma and Laves phases. This corresponds to the phase formation sequence predicted for the cast alloy.

As compared to the cast material, the preparation of PM alloy consisted of heating the solid powders with already homogenous chemical composition to 1100 °C sintering temperature, short dwell time and relatively rapid cooling. In accordance with the thermodynamic prediction, FCC solid solution, ordered FCC $L1_2$ and BCC were experimentally observed in the powder metallurgy (PM) HEA (later confirmed by TEM), in which the solid-state sintering took place at 1100 °C. Despite the predicted liquid phase present at 1100 °C, no melting was observed during sintering. This could be a consequence of short sintering time and high pressure which may increase the melting temperature. The phase composition formed at 1100 °C was then retained to room temperature due to relatively rapid cooling after sintering, preventing nucleation and growth of Laves and sigma (σ) precipitates. As seen in Fig. 1b, the temperature of the first stable equilibrium occurrence of sigma (σ) phase of this particular alloy during cooling is 883 °C. However, our sintering temperature was carried out in a rapid heating rate of 100 $°C{\cdot}min^{-1}$ up to 1000 °C, and then slowed down to 50 $°C{\cdot}min^{-1}$ up to the final temperature of 1100 °C, followed by a relatively rapid cooling after the sintering.

Due to the short processing times (fast heating and cooling), the nucleation of sigma (σ) phase in the PM alloy was avoided; in other words, the time spent in the temperature range at which effective diffusion would allow for sigma phase nucleation and growth was not sufficiently long.

This is in accordance with other studies: the kinetics of nucleation of the sigma phase was observed to be extremely slow in HEAs [35], particularly in FCC ones containing Ni. The reason is that nickel acts as a strong stabilizer of the FCC solid solution, suppressing the formation of the Cr-rich σ phase. In fact, the σ phase was shown to be formed in the $CrMnFeCoNi_x$ alloy only after annealing at 700–900 °C for $>$1000 h.

Similarly, the temperature for formation of Laves phase during cooling is about 793 °C. Therefore, the formation of Laves phase did not take place as well. On the other hand, the nucleation of ordered FCC $L1_2$ phase took place due to the slower heating rate (50 $°C{\cdot}min^{-1}$) from 1000 °C up to the maximum temperature of 1100 °C.

The thermodynamic calculation was also in good agreement with the phases detected in the Cast HEA: FCC disordered, BCC, Laves and σ. The latter two phases most likely precipitated during cooling at temperatures below 800 °C. The ordered FCC $L1_2$ might either not have formed in the structure or may not have been detected in the alloy due to having content below the detection threshold of the techniques used for phase analysis (XRD + EBSD). It should be noted that the occurrence of a certain segregation is expected in the cast alloy due to liquid-solid transformation. On the other hand, segregation effects are completely omitted in PM HEA due to solid-phase processing.

It should be pointed out that some discrepancies between calculations and experiments may always arise due to the real nature of the materials' experimental conditions—as they may be in a state close to equilibrium but may also contain metastable phases. The phase diagrams are essentially calculated for a thermodynamic equilibrium state characterized by a global minimum of Gibbs energy [36]. Experimentally, this could only be reached by extremely slow cooling conditions or prolonged annealing times [37]. On the other hand, our experimental materials were cooled rapidly, avoiding the formation of some phases.

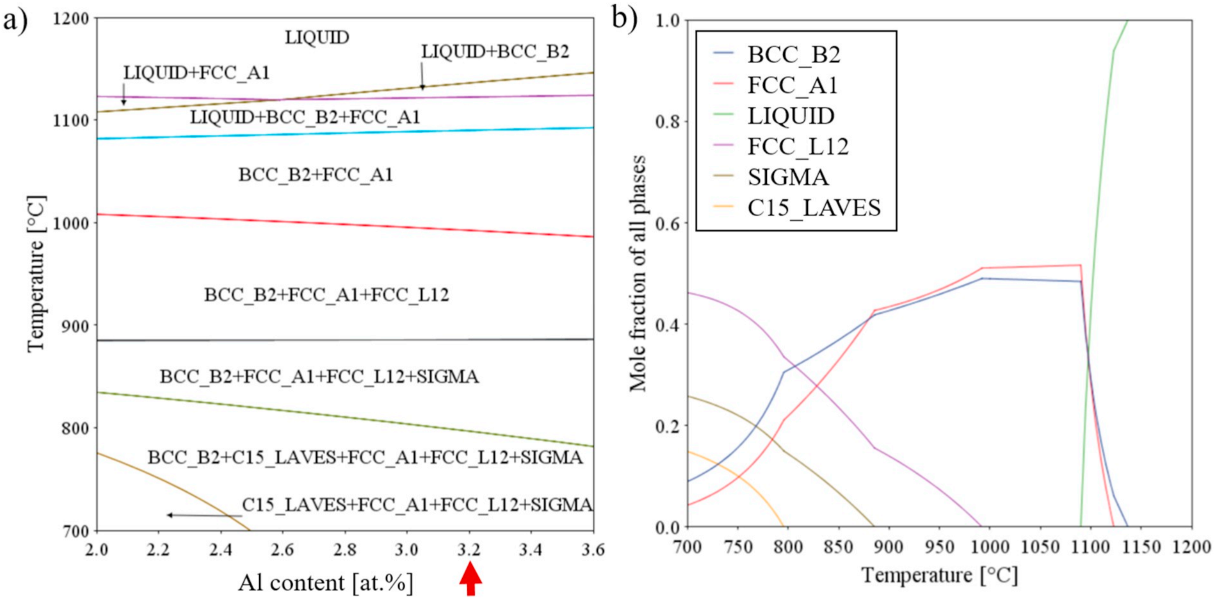

Fig. 1. CALPHAD calculations for the studied HEA. a) $Al_xCo_{1.5}CrFeNi_{1.5}Ti$ calculated phase diagram in the range from $2.0 < x < 3.6$. The investigated alloy composition ($x = 3.2\%$) is marked with the red arrow. b) Property diagram of $Al_{0.2}Co_{1.5}CrFeNi_{1.5}Ti$ as mole fraction of all phases vs. temperature. (For interpretation of the references to color in this figure legend, the reader is referred to the web version of this article.)

3.2. Microstructural characterization

The XRD pattern analyses of the two $Al_{0.2}Co_{1.5}CrFeNi_{1.5}Ti$ alloys produced by powder metallurgy and casting are provided in Fig. 2. After mechanical alloying and SPS densification, the PM HEA (Fig. 2) comprises a major FCC solid solution matrix with lattice parameter of 3.58 Å. The volume fraction of the matrix was estimated to be 89.3%. The peaks of the second most dominant phase were attributed to TiC with lattice parameter a = 4.30 Å and 8.0% in volume fraction. Additional peaks in the pattern conforming to the remaining 2.7% fraction of the microstructure correspond to a BCC phase with lattice constant a = 2.93 Å.

The patterns for the cast alloy show the formation of a more complex multi-phase microstructure (Fig. 2), as compared to the PM HEA, with FCC solid solution again as the predominant phase. Additionally, Laves, sigma and BCC phases were detected. The FCC solid solution matrix in the Cast HEA possess a lattice parameter of 3.63 Å and 47.8% volume fraction.

The second most dominant phase in the Cast HEA is the intermetallic Laves phase with lattice parameters a = 4.79 Å and c = 7.79 Å and a 30.8% calculated volume fraction. Moreover, a sigma phase was present with lattice constants a = 8.88 Å and c = 4.57 Å and a fraction of 11.5%. Importantly, Laves and sigma phases were not present in PM HEA. The remaining volumetric fraction of 10.1% is attributed to BCC with lattice constant a = 2.93 Å, i.e., same as in PM HEA.

The peaks for TiC were detected only for the PM HEA, demonstrating that carbide formation is thermodynamically favourable during the powder milling process due to the nature of the technique, as previously reported in [38]. As carbon was not initially present in the feedstock powders, the decomposition of the toluene used as a milling agent for preparing powders for PM HEA should be regarded as its source. Consequently, an in-situ reaction of carbon and titanium took place, owing to their having the highest chemical affinity among the used elements.

The lattice constants of the alloys were determined by XRD and by selected area electron diffraction patterns (SAEDP) from TEM analysis (Table 1). A lattice-parameters comparison of the respective phases of each alloy indicates that they possess analogous FCC matrices and BCC phase in common.

The microstructure of the PM alloy is presented in Fig. 3 (FCC matrix and its features) and Fig. 4 (BCC and carbides). The FCC solid solution matrix can be seen in Fig. 3a, combined with its respective SAEDP (Fig. 3b) along the [011] zone axis, confirming the lattice constant as a = 3.61 Å, i.e., in good agreement with the XRD results (Table 1). The EDX point analysis indicates a matrix rich in Fe, Ni and

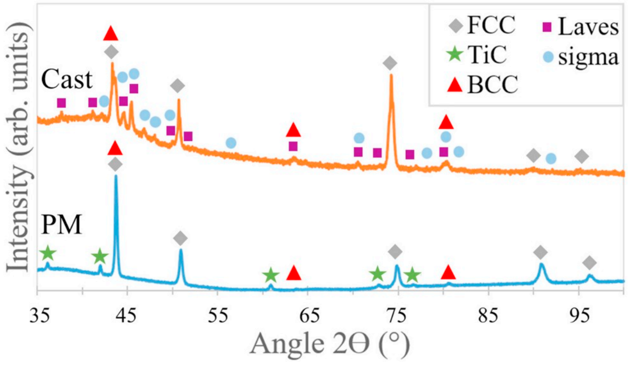

Fig. 2. XRD patterns and phase composition of PM HEA after the SPS densification (blue – PM) and Cast HEA (orange – Cast). (For interpretation of the references to color in this figure legend, the reader is referred to the web version of this article.)

Table 1
Comparison of lattice parameters of PM and Cast HEA measured by XRD and selected area electron diffraction (SAEDP). The volume fractions of each phase are exhibited in bold.

	a_{XRD}	c_{XRD}	a_{SAED}	c_{SAED}	Vol%
PM HEA [Å]					
FCC matrix	3.58	3.58	3.61	3.61	**89.3**
TiC	4.30	4.30	4.38	4.38	**8.0**
BCC	2.93	2.93	2.95	2.95	**2.7**
Cast HEA [Å]					
FCC matrix	3.63	3.63	3.67	3.67	**47.8**
Laves	4.79	7.79	4.75	7.73	**30.8**
Sigma (σ)	8.88	4.57	8.82	4.61	**11.5**
BCC	2.93	2.93	2.92	2.92	**10.1**

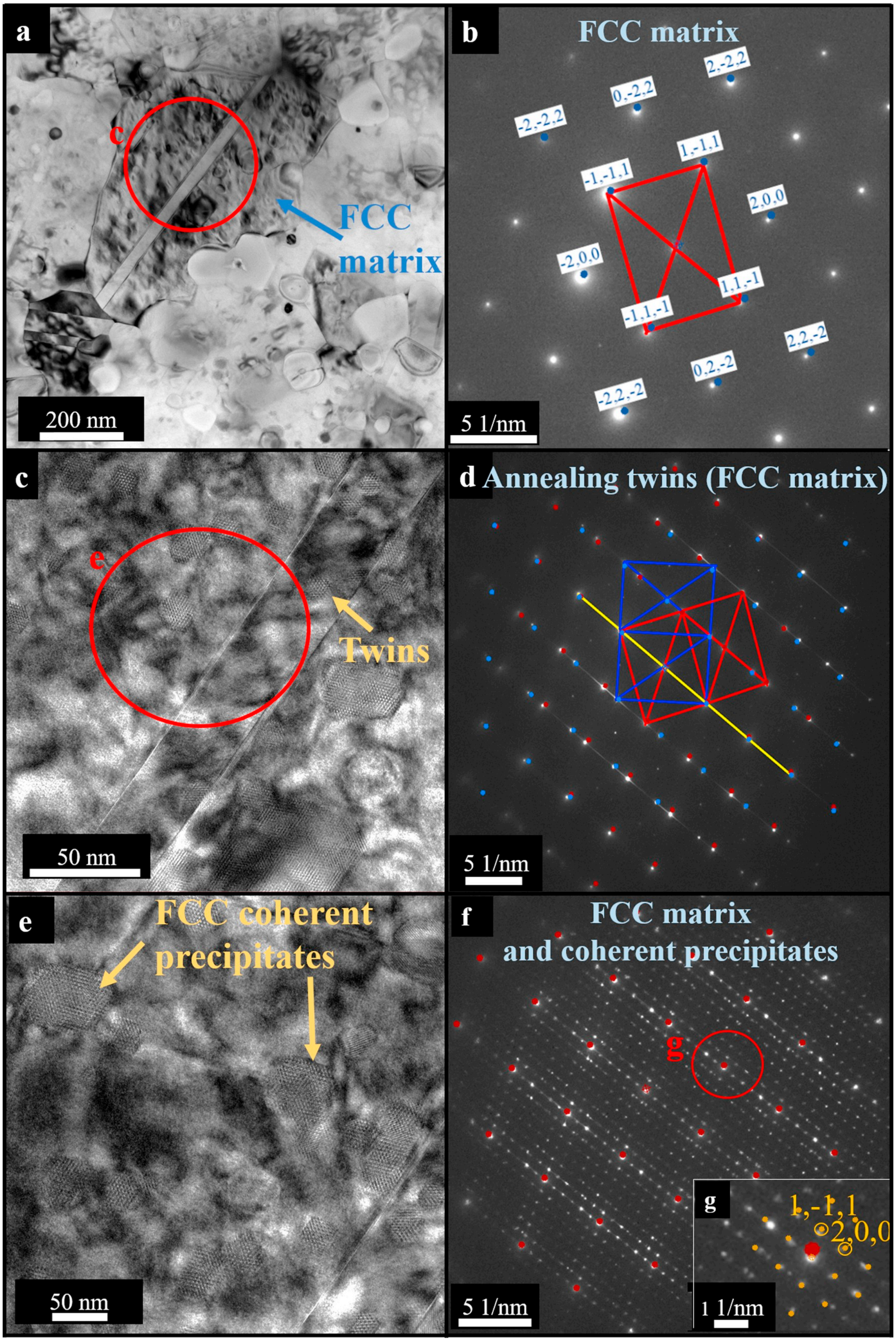

(caption on next page)

Fig. 3. Bright-field TEM image of the $Al_{0.2}Co_{1.5}CrFeNi_{1.5}Ti$ PM HEA on the left side and SAED patterns of the respective phases on the right side. a) FCC matrix. b) SAEDP along the [011] zone axis. c) Twin boundary representation within the FCC matrix. d) SAEDP of a twin - the red dots are a simulation of the corresponding planes along the zone axis [011]. The blue dots are the representation of twins through reflection planes. e) Nano-precipitates coherent with FCC matrix. f) SAEDP of the FCC matrix showing coherent precipitates along zone axis [011]. A schematic simulation of the pattern of FCC matrix is represented by red dots. g) Coherent ordered FCC phase represented by yellow dots surrounding the reflection from the FCC matrix (red dot). (For interpretation of the references to color in this figure legend, the reader is referred to the web version of this article.)

Co (Table 2).

Annealing twins have been observed within the FCC matrix (Fig. 3c) and further confirmed by SAEDP (Fig. 3d). The additional spots of the SAEDP correspond to patterns simulated for FCC twins with 60° misorientation to the matrix. The twins are represented by blue dots through the reflection planes on the ⟨011⟩ direction by 70.53° [39,40].

The occurrence of such annealing twins formed due to the high-temperature exposure of the material during SPS points out to the low stacking fault energy (SFE) of the FCC matrix, as the twinning boundary represents a long stacking fault (analogous to FCC austenitic steels [41]). The annealing twins are generated during recrystallization of the mechanically alloyed powder microstructures [28,42] at the sintering temperature.

The presence of nano-sized coherent precipitates within the FCC matrix in the PM alloy is documented in Fig. 3e and confirmed by the SAED patterns along the zone axis [011] in Fig. 3f. The coherent ordered FCC phase is represented by a simulation of the supercell reflections (yellow dots) surrounding the reflection of the FCC matrix (red dot) in Fig. 3g inset. The supercell has a lattice constant about five times larger than the matrix. The coherent precipitates should correspond to Ni_3Ti precipitates with $L1_2$-type ordered lattice structure, as predicted by CALPHAD (Fig. 1).

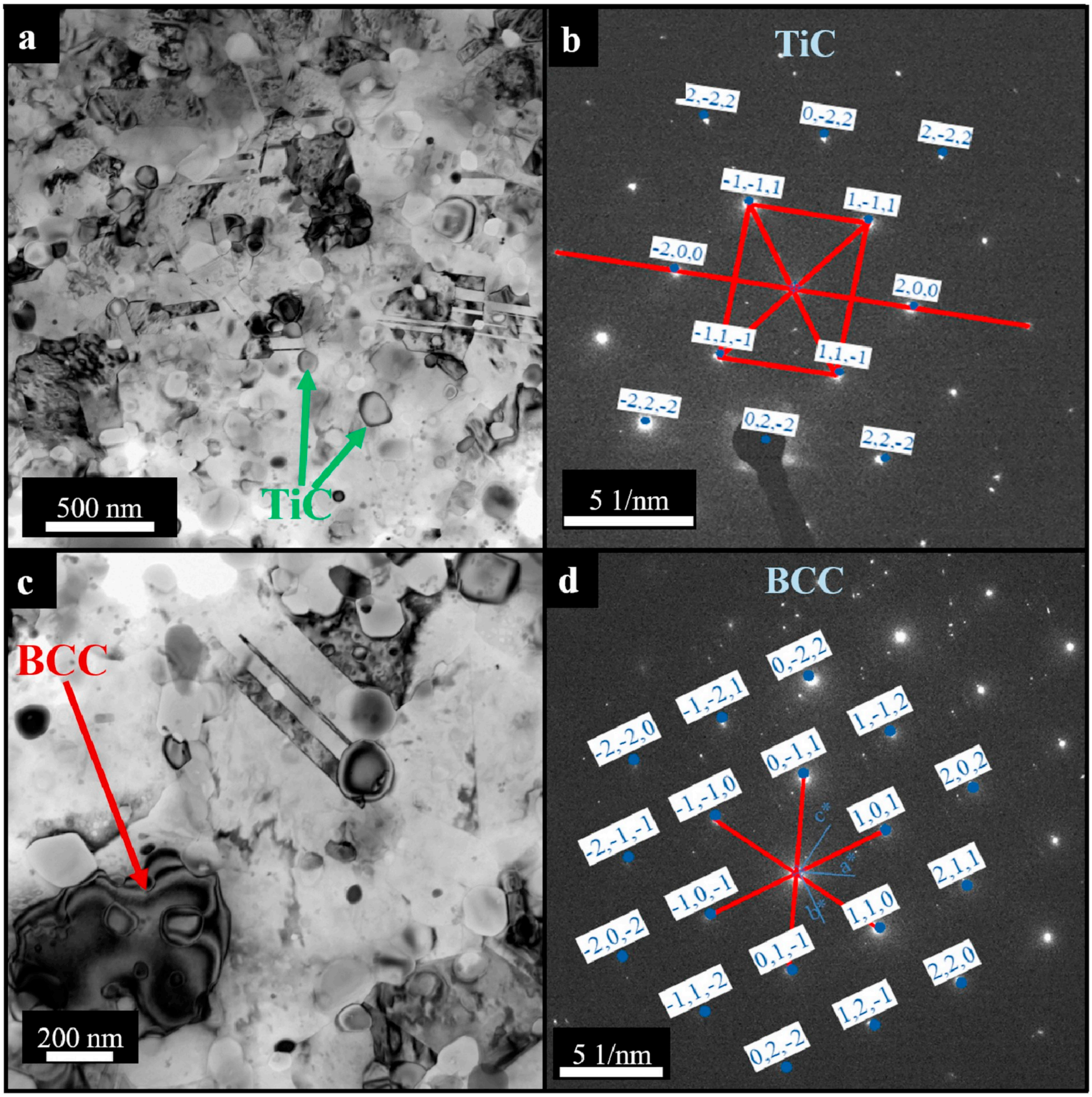

Fig. 4. Bright-field TEM image of $Al_{0.2}Co_{1.5}CrFeNi_{1.5}Ti$ PM HEA on the left side and SAEDP of the respective phase on the right side. a) Dispersed TiC within the matrix. b) SAEDP from PM HEA of TiC along [011] zone axis. c) Representation of BCC phase. d) SAEDP from PM HEA along [−111] zone axis of BCC.

Table 2
Comparison of the EDX chemical composition of the PM and cast alloys. The main elements of each phase are emphasized in bold.

Chemical composition [at.%]									
Phase	FCC matrix		BCC		TiC	Laves	σ phase	Map sum spectrum	
Alloy	PM	Cast	PM	Cast	PM	Cast	Cast	PM	Cast
Al	9.2	7.4	4.1	7.0	0.5	1.3	5.4	3.8	3.3
Ti	3.6	16.8	**19.3**	**23.5**	**92.6**	**28.0**	7.1	15.4	15.0
Cr	10.1	15.4	3.7	4.4	1.4	1.2	**28.2**	14.5	14.5
Fe	**20.3**	**17.1**	9.8	10.9	2.2	1.9	**24.1**	15.8	16.1
Co	**28.1**	**24.4**	**31.2**	**25.8**	1.8	**21.4**	**20.2**	24.4	24.4
Ni	**28.6**	**19.1**	**32.0**	**28.5**	1.5	**46.2**	14.9	26.1	26.7

Nano-sized coherent precipitates were formed by precipitation from the FCC matrix while cooling after sintering. The mentioned precipitation phenomena can be related to the coherent $L1_2$ phase formation (γ') in the matrix, which may eventually be transformed to η-phase as previously reported on similar HEAs [26,43], forming a γ/γ' relationship with the matrix. This phenomenon is analogous to one observed in traditional Ni-base superalloys.

The globular TiC particles formed in-situ during milling are characterized in Fig. 4a and Fig. 4b. The SAEDP along the [011] zone axis shows an ordered FCC structure with lattice parameter a = 4.38 Å, corroborating the a = 4.30 Å values obtained by XRD (Table 1). The TiC structure was first reported in [44], in which the lattice constant was found to be smaller, a = 3.32 Å, according to the Inorganic Crystal Structure Database (ICSD) collection code 44494. The EDX point analysis has confirmed that the phase is Ti-rich (Table 2). This was further supported by the mapping presented in the supplementary material Fig. S1, clearly showing globular-like areas rich in Ti.

The minor BCC phase (2.7 vol% fraction) in the PM alloy is shown in Fig. 4c and its respective SAEDP along the [−111] zone axis is shown in Fig. 4d with the calculated lattice parameter of a = 2.95 Å comparable to the results extracted from XRD (Table 1). The phase is rich in Ni, Co and Ti (Table 2 and an additional EDX map provided in the supplementary material Fig. S2).

The microstructures of the Cast HEA variant and their respective SAEDPs are presented in Fig. 5 (patterns of the major FCC and Laves phases) and Fig. 6 (minor phases: σ and BCC).

Fig. 5a shows typical microstructural features of the cast alloy, in which the FCC matrix surrounded by elongated needle-like Laves and σ phases, and very fine dispersed globular BCC precipitates can be observed.

The SAED patterns of the FCC matrix along [−110] zone axis in the Cast HEA are displayed in Fig. 5b. The phase is (Fe, Ni, Co)-rich and with a calculated lattice parameter a = 3.67 Å, confirming the values from XRD peaks (Table 1).

The Laves phase was only present in the cast alloy and is depicted in Fig. 5c. Its SAEDP along the [11–20] zone axis is shown in Fig. 5d. The lattice constant for this topologically close-packed (TCP) phase was calculated to be a = 4.75 Å and c = 7.73 Å, in accordance with the XRD results, a = 4.79 Å and c = 7.79 Å, presented in Table 1. The phase is rich in Co, Ni and Ti corresponding to a ratio $(Co, Ni)_2Ti$, as shown in Table 2 and confirmed by EDX maps of the corresponding areas marked by red arrows in supplementary material Fig. S3.

The σ phase (11.5 at.%) found only in the Cast HEA is denoted by the green arrow in Fig. 6a. Its SAEDP together with the simulated pattern along the [100] zone axis for the phase depicted in Fig. 6b have lattice constants a = 8.82 Å and c = 4.61 Å. Similar results were obtained by XRD diffraction peaks (Table 1). This phase is rich in Cr, Co and Fe (Table 2). The EDX maps (Fig. S3 supplementary material) also show the presence of the same elements in the indicated areas pertaining to the σ phase, as marked by the blue arrows. In HEAs, Cr has been repeatedly reported to promote the formation of the σ phase, particularly in the presence of Fe, Co, and Ni [45].

The minor BCC phase (10.1 at.%) also present in the Cast HEA is depicted in Fig. 6c, marked with the blue arrow. Its lattice constant was measured by SAEDP (Fig. 6d) along the [111] zone axis, showing a = 2.92 Å, i.e., matching the equivalent result of a = 2.93 Å found by XRD, and the same BCC minor phase as in the PM counterpart (Table 1). The similarities between the BCC phase in the PM and cast alloys are also evidenced by the analogous chemical compositions shown in Table 2, both being Ni-, Co- and Ti-rich.

The PM and Cast HEAs possess identical overall chemical compositions, as established by area EDX TEM mapping (Table 2), matching the $Al_{0.2}Co_{1.5}CrFeNi_{1.5}Ti$ stoichiometric ratio. Both the PM and cast FCC matrices are Fe-, Ni- and Co-rich (Table 2). The difference in the chemical composition of both alloys lies in the Ti partitioning. In the cast alloy, the FCC matrix phase is rich in Ti, while in the PM alloy, Ti is depleted. In the PM HEA, Ti reacted with C to form TiC, thereby depleting the FCC matrix of Ti. These said, the differences in microstructures must be solely a result of different processing routes and temperature profiles. Furthermore, the TEM results for both PM and Cast HEAs are in good agreement with the calculated phase diagram computed by CALPHAD and XRD.

For quantitative evaluation of the microstructure, EBSD analyses have been performed, with results concerning the phase distribution, orientation and grain sizes of the PM and cast alloys presented in Figs. 7 and 8, respectively.

With the SPS-process, full density fine-grained samples can be produced, even at relatively short sintering periods (10 min). The PM alloy possesses a distribution of fine nano-sized grains of both FCC and TiC (Fig. 7a, c, d). The average grain sizes of the FCC matrix and TiC are 0.42 μm and 0.40 μm, respectively. The fine grain size is attributed to the high thermal stability of the TiC particles, which prevented grain growth of the FCC matrix by grain boundary pinning and a consequence of the SPS rapid densification (short sintering time) of the severely plastically deformed (i.e., grain refined) mechanically alloyed powders.

One can perceive the random orientation of both FCC and TiC grains despite the uniaxial pressing during the SPS of the PM alloy, as any type of preferential crystallographic texture cannot be detected in Fig. 7b. Due to EBSD resolution constraints, the BCC phase is not visible.

In contrast to the PM alloy, the cast alloy presents a much larger average grain size distribution (Fig. 8a, c). The quantitative analysis of the FCC matrix and Laves phases shows that their average grain size is 42.8 μm and 5.4 μm, respectively.

The large-sized grains of the cast alloy essentially show one preferential crystallographic orientation due to dendritic solidification (Fig. 8a). Due to the heterogeneous nucleation, the dendrites crystalize in specific directions of heat dissipation at the ingot mould sides, a phenomenon seen often in metallic castings. Consequently, the FCC phase has a very strong orientation texture (Fig. 8b), as opposed to the essentially texture-free PM alloy. The same strong crystallographic orientation applies to the Laves phase.

The white regions in the EBSD maps correspond to non-indexed areas that were impossible to resolve accurately due to the resolution threshold of the method. They may possibly correspond to a mixture of nano-sized phases already identified in the TEM images (namely σ, BCC, or the needle-like nano-sized Laves phase, documented in Fig. 6a).

In an overall comparison of the PM and Cast HEAs microstructures, combining mechanical alloying and SPS seems to deliver better results than casting, even considering the presence of carbide particles. The PM process produced a significantly more refined, uniform and chemically homogenous microstructure essentially without preferential orientation and porosity. To obtain a comparably uniform microstructure, the Cast HEA would have to be subjected to additional procedures (homogenization combined with hot working or cold working). However, such methods would further complicate the materials' processing due to the needed plastic deformation (change of shape) and would unnecessarily increase the cost of production. Additionally, the hot and

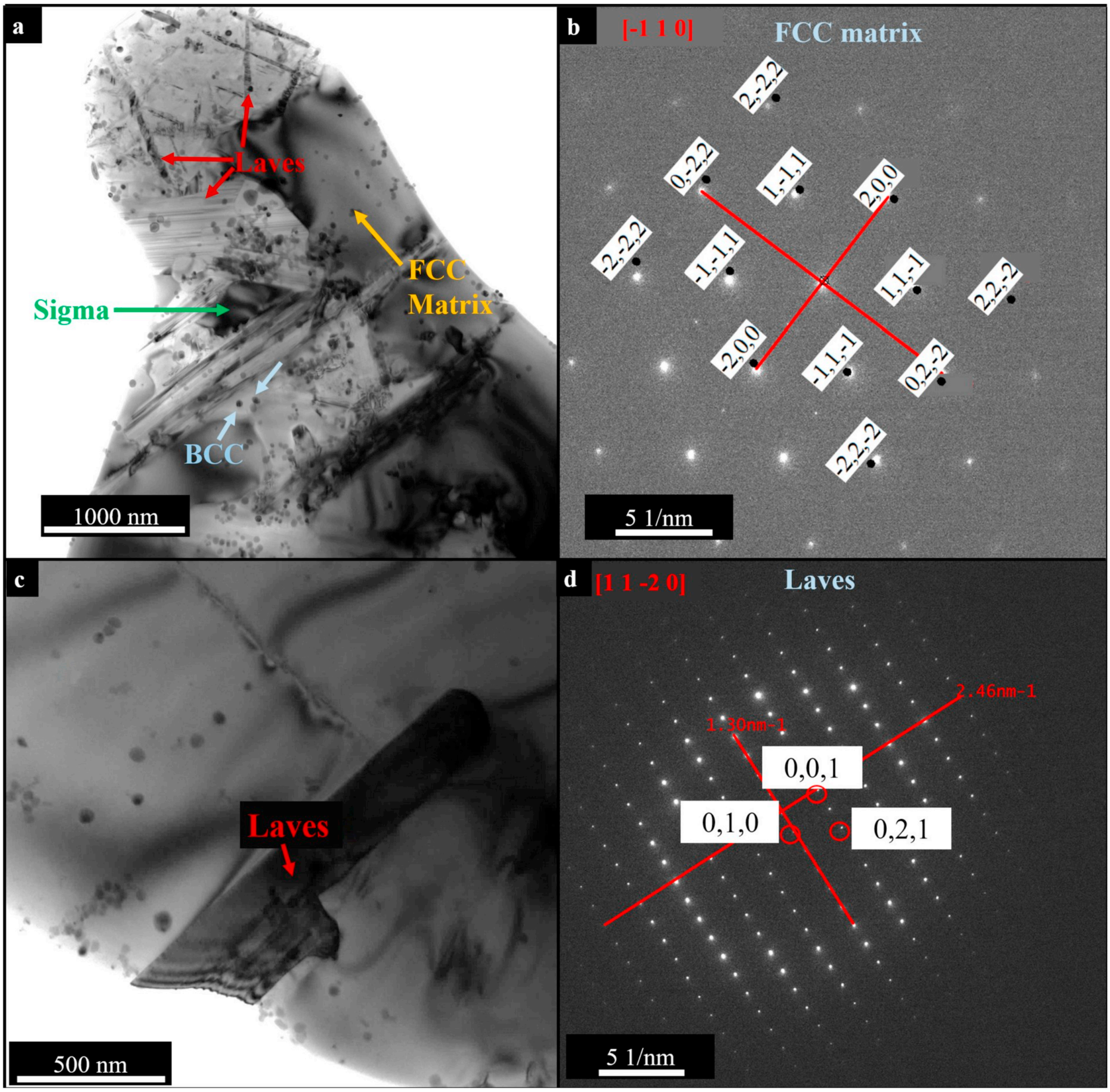

Fig. 5. Bright-field TEM image of the $Al_{0.2}Co_{1.5}CrFeNi_{1.5}Ti$ Cast HEA on the left side and SAEDP of the respective phase on the right side. a) Representative microstructure showing all phases present in the alloy. b) SAEDP of the FCC matrix along [− 110] zone axis. c) Needle-like Laves phase. d) SAEDP of the Laves phase along [11–20] zone axis.

cold workability of this Cast HEA with such a significant volume of brittle TCP phases is questionable.

3.3. *Mechanical properties*

3.3.1. *Hardness and bending strength*

The results of mechanical characterization by means of hardness and bending testing are presented in Table 3. The hardness values obtained by Vickers test for PM and Cast HEAs were found to be 712 ± 3 HV and 682 ± 10 HV, respectively. The elastic modulus E of each material was measured by nanoindentation test. The results show that the PM HEA possesses E modulus of 258 ± 10 GPa, while the cast counterpart shows ~22% lower value of E = 210 ± 10 GPa. The slightly higher PM HEA E modulus can be attributed to the presence of very stiff TiC, which possesses alone an E modulus = 400 GPa [46]; therefore, contributing for the overall E of the material.

The bending strength (R_{mo}) of the PM material was exceptionally high, with values exceeding 2 GPa (averaging 2018 ± 65 MPa). These values are almost double compared to the Cast HEA, which has an average R_{mo} of 1101 ± 42 MPa.

The reasons for the great differences in mechanical response between both materials are primarily explained by their particular microstructural characteristics. Except for TiC formation in the PM alloy, no significant inclusions, segregation of elements or porosity were detected in both alloys, suggesting these do not play a role in the mechanical properties (cf. Figs. S7 and S8 – supplementary material).

The better mechanical properties of PM HEA stem from the advantages of a more uniform microstructure. Additionally, the remarkably high strength is attributed to Hall-Petch strengthening. PM HEA exhibits a much smaller grain size in all phases, with nanosized grains (0.42 μm) of the FCC matrix holding 89.3% of the total volume and additional TiC particles pinning the grain boundaries.

On the other hand, the cast alloy's mechanical performance was inferior to the PM HEA, due to a much more heterogeneous microstructure. Even though the cast alloy's larger FCC matrix grains (42.8 μm) should be more ductile (compared to the nano-grained PM

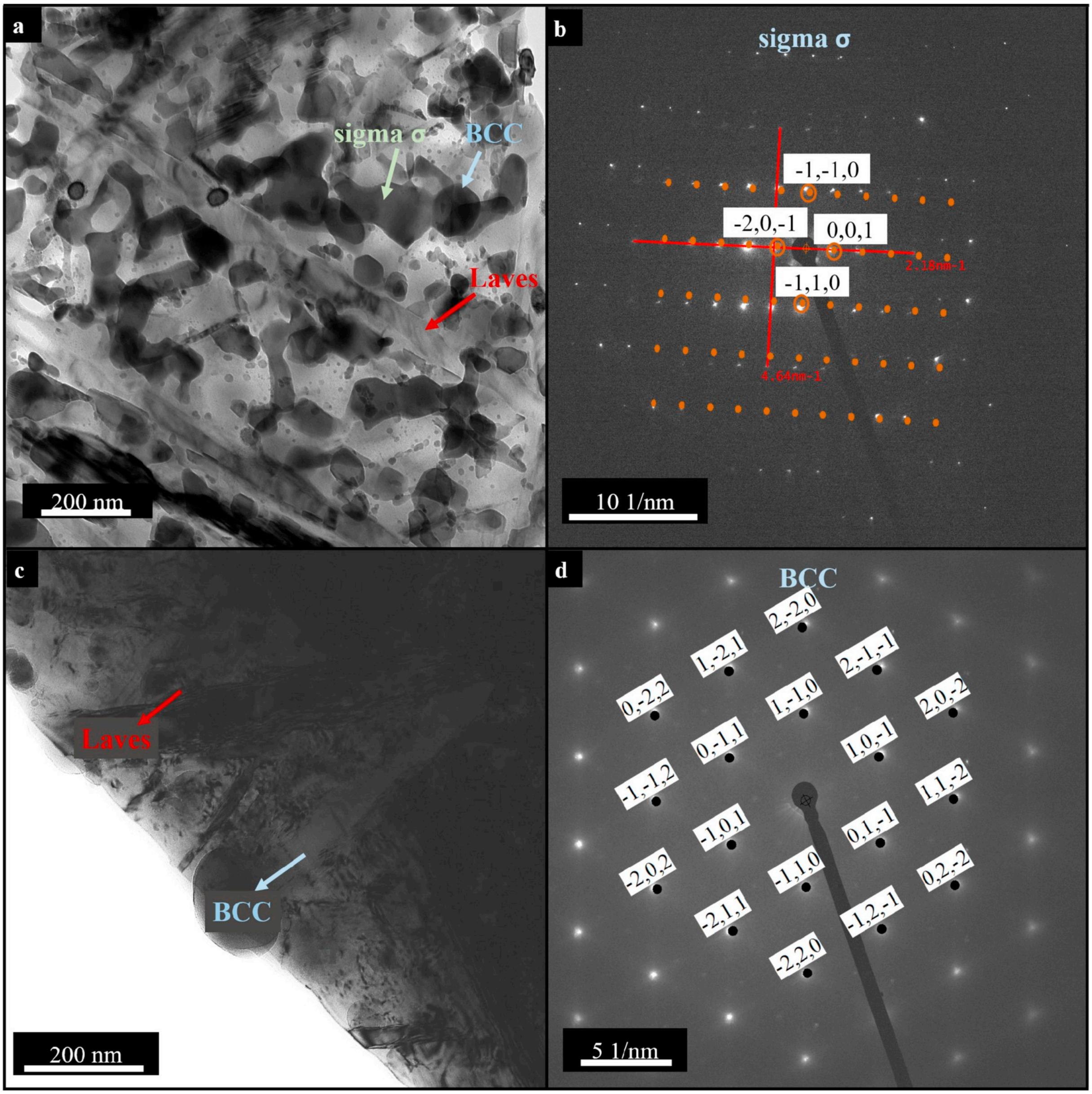

Fig. 6. Bright-field TEM image of the $Al_{0.2}Co_{1.5}CrFeNi_{1.5}Ti$ Cast HEA on the left side and SAED patterns of the denoted phase on the right side. a) Representative TEM image showing Laves, σ and BCC phases. b) SAEDP of σ phase along [100] zone axis. c) Typical microstructure for needle-like Laves and BCC phases. d) SAEDP of BCC along [111] zone axis.

HEA), a brittle behaviour was observed. This is caused by a high volume fraction of brittle σ and Laves phases (52.4%) in the Cast HEA, possessing very brittle TCP crystal structures combined with minor BCC nanoparticles - which in turn have a significant detrimental effect on the mechanical response.

Neither material showed any significant plastic strain, i.e., their failure occurred immediately after the initial elastic loading. In the case of PM, this occurred due to its extremely high strength and therefore insufficient plasticity, while, for the cast counterpart, due to the intrinsic brittleness caused by intermetallic phases.

The results of the fractographic analysis of the ruptured bending test specimens are presented in Fig. 9.

The morphology of the fracture surface of the PM alloy is a mixture of ductile and brittle fracture mechanisms. The presence of very fine and shallow ductile dimples, shown in Fig. 9a, is attributed to the small grain size of the ductile FCC matrix present in a high volume fraction.

No visible inclusions or other particles were detected inside the dimples, suggesting a strong metallurgical bonding of the TiC particles with the matrix (Fig. 9b). The absence of particles inside the dimples suggests that, most likely, the crack initiated and propagated by ductile tearing inside the FCC matrix, forming a dimple-like surface morphology formed by adjacent microvoid coalescence [47].

Considering that no significant ductility was present during the bending, the fracture possesses a transgranular character and should be referred to as brittle in nature, frequently called low-energy tearing [47,48], despite the presence of ductile dimples. The fracture surface contains ridges retracting towards the fracture initiation site as shown in Fig. 9c, a morphology typical for brittle fracture behaviour.

The lack of macroscopic ductility for the PM HEA might be explained by the severely strengthened microstructure. Nano-grains are a consequence of the high strains that the material was subjected to during its milling in powder state, followed by incomplete recrystallization during the sintering processing times. The grains were further pinned by an in-situ formation of the TiC particles. This effect is

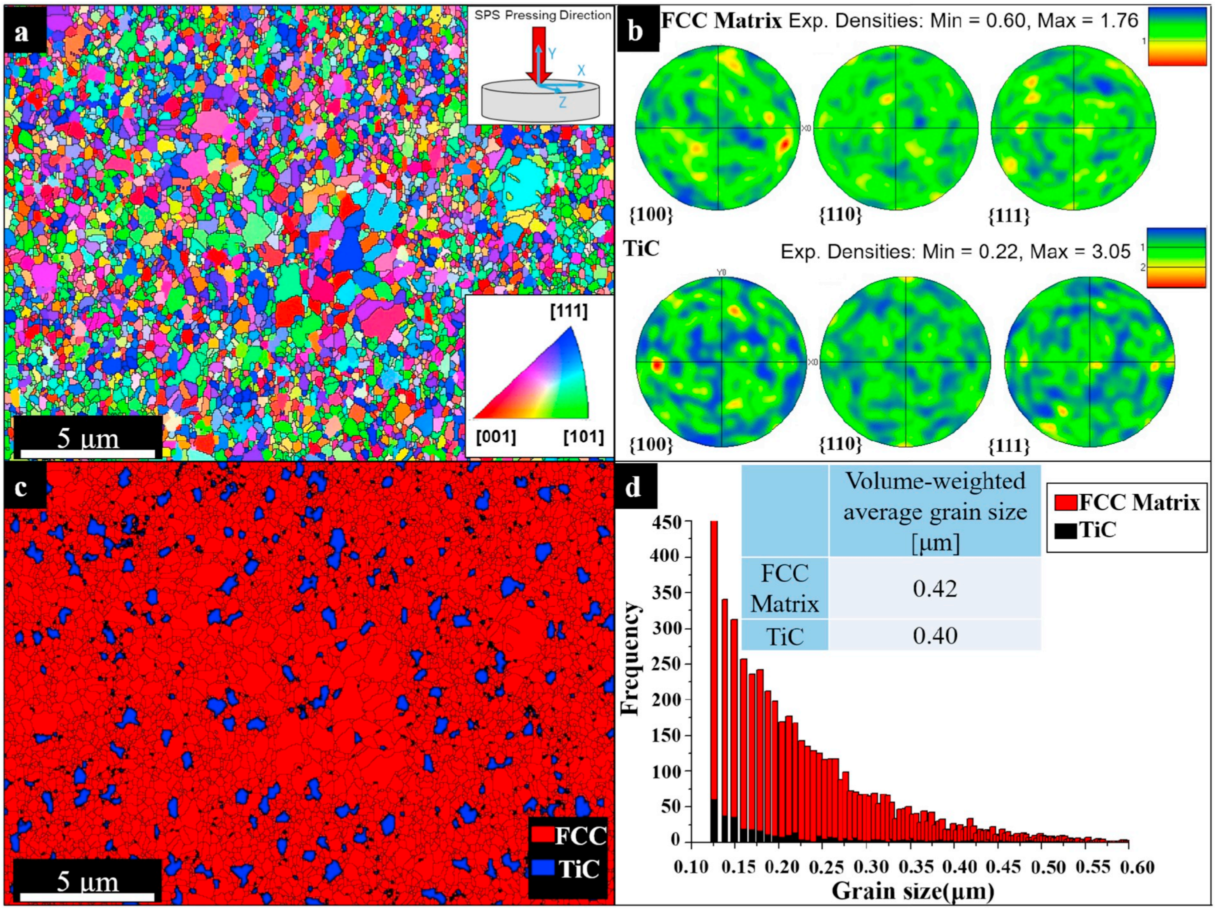

	Volume-weighted average grain size [µm]
FCC Matrix	0.42
TiC	0.40

Fig. 7. Representative SEM EBSD analysis of the PM HEA. a) Inverse pole figure showing grain orientation maps with reference direction perpendicular to the SPS compaction direction denoted as Z in the image. b) Pole figures of FCC and TiC phases. c) Phase map showing distribution of TiC in FCC matrix. d) Grain size distribution of respective phases with average grain size and volume fraction.

common for high-strength alloys, where dislocation motion is severely restricted [49,50], even though ductile fracture by microvoid coalescence with ductile dimples of various sizes occurs.

Compared to PM HEA, the Cast HEA manifested a considerably pronounced brittle nature of the fracture surface morphology, with comparably larger cleavage facets corresponding to brittle phases cracking (Fig. 9d). The green arrow shows a typical total cleavage separation of a brittle phase. Some of the brittle facets are surrounded by ductile fracture of the FCC matrix (Fig. 9e), in which the deformation creates a ductile bridge between the facets, preceding the fracture by cleavage.

The yellow arrows in Fig. 9d point to the formation of cleavage steps in the crack propagation along different crystallographic planes for dissipation of deformation energy. This is a consequence of the presence of different nano-sized particles within the matrix, interacting with the crack tip and changing the cleavage step mechanism.

The cast material does not exhibit a major initiation site (Fig. 9f) but rather evidences multiple initiation sites from the surface. A typical initiation site is marked in yellow. The existence of a high volume fraction of brittle secondary phases (52.4% of the total volume calculated from XRD patterns) is responsible for the exceptionally brittle character of the Cast HEA fracture.

3.3.2. Wear tests

The specific wear rates of the PM and Cast HEAs were compared with the reference AISI 52100 (conventional wear-resistant steel) and Inconel 713. The latter possesses a microstructure similar to that of PM HEA, containing fine coherent precipitates dispersed within the FCC matrix. The results are shown in Fig. 10.

The corresponding values of the worn volumes, as well as the average coefficients of friction (COF) recorded in-situ, are provided in Table 4. The variations in the specific wear rates are directionally proportional to the worn volume of material and inversely proportional to the force applied; both values will, therefore, be provided.

Among all tested materials, the Cast HEA had the best performance under both loading conditions, possessing specific wear rates of 1.6×10^{-8} $mm^2 \cdot N^{-1}$ for 1.2 N (corresponding to a worn volume of material of 0.71 μm^3 and COF = 0.67 ± 0.11) and 2.5×10^{-8} $mm^2 \cdot N^{-1}$ for 5 N (a worn volume of 1.07 μm^3 and COF = 0.67 ± 0.04). The maximum contact pressures between the sphere and the flat surface were calculated to be 0.51 GPa and 0.83 GPa, respectively. Surprisingly, in comparison with the traditionally used wear-resistant AISI 52100, the performance of the Cast HEA was remarkably higher, achieving a specific wear rate ten times lower than AISI 52100.

The PM HEA exhibited results slightly superior to the traditional AISI 52100 under 1.2 N load, as its specific wear rate was found to be 7.5×10^{-8} $mm^2 \cdot N^{-1}$ and COF = 0.74 ± 0.08. The worn volume was calculated to be 3.25 μm^3, i.e., about 4.6 times higher than the worn volume of its cast counterpart.

Under higher loads, the PM material seems to become more fragile. The contact pressures under the two loads were calculated to be 0.55 GPa and 0.88 GPa, respectively, i.e., values similar to the ones encountered for the Cast HEA. Above 0.55 GPa, the microstructure can no longer withstand higher loads and the wear rate substantially increases from 7.5×10^{-8} $mm^2 \cdot N^{-1}$ up to 1.1×10^{-6} $mm^2 \cdot N^{-1}$, a value

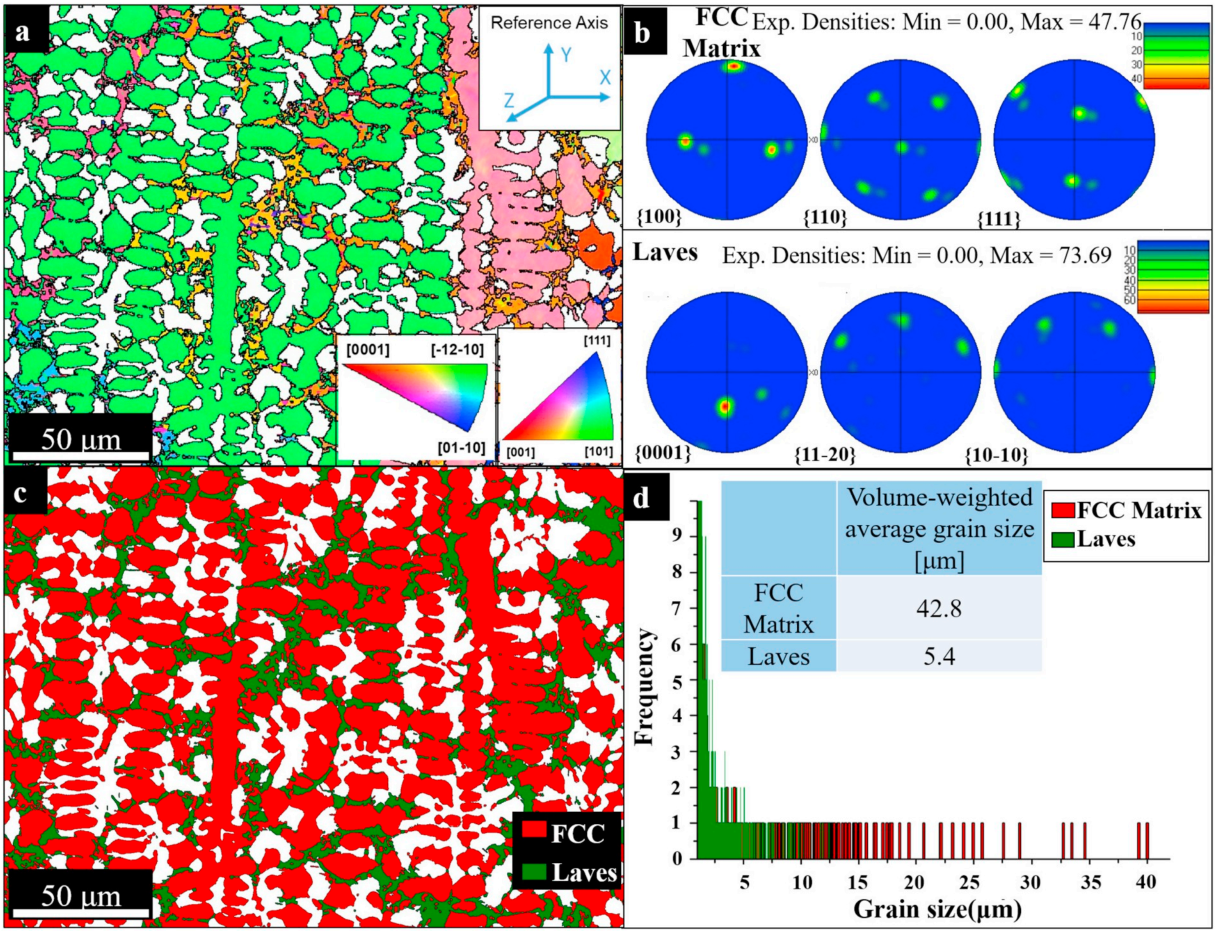

Fig. 8. Representative SEM EBSD analysis of the Cast HEA. a) Inverse pole figure orientation map with reference direction Z denoted in the image. b) Pole figures of FCC and Laves phases. c) Phase map showing distribution of Laves in FCC matrix. d) Grain size distribution of respective phases with average grain size and volume fraction.

Table 3
Average hardness, elastic modulus and flexural strength for the PM and Cast HEAs.

	Hardness [HV]	E [GPa]	R_{mo} [MPa]
Cast	682 ± 10	210 ± 10	1101 ± 42
PM	712 ± 3	258 ± 10	2018 ± 65

almost 15 times higher. Consequently, the corresponding wear volume exhibited a significant increase to 48.57 μm^3. The respective COF equals 0.60 ± 0.04, i.e., lower than that at 1.2 N load.

In general, both PM and Cast HEAs showed very good wear resistance under a 1.2 N load, superior to the commercially available AISI 52100 or Inconel 713 materials.

The overall morphology of the wear surface for both PM and cast alloys can be seen in Fig. 11. Three-dimensional optical profilometry images of the worn tracks show the individual grooves and plastic deformation. Those features represent broken adhesive junctions on the worn surface.

The deep grooves on the surfaces could be associated with delamination wear [51,52] that originates from severe plastic deformation in the contact of asperities. The resulting plastic shear strain is accumulated in the subsurface layer, and when it reaches a certain value, cracks are formed and material is removed in the form of flake-like particles.

There are significant differences in the wear rate between the PM and the Cast HEA (already revealed in Fig. 10). As shown in Fig. 11, especially at higher load, the wear track of the PM HEA is much more deeply grooved and the adhesive material transfer process is more evident. In contrast, the wear track is much narrower. This indicates very severe adhesive wear in a smaller area due to the significant material transfer in the initial point contact.

EDX analysis on the worn surface features of broken adhesive junctions (provided in supplementary material – Figs. S2, S3 and Table S1.) reveals a high content of iron oxides, which, together with the test conditions, indicates a mild-oxidational wear regime [51]. A relatively high Fe content suggests that the material partially originates from the counterpart ball.

Important variations in friction response for each material may be triggered by large differences in microstructures; average grain sizes and distribution; phase composition and respective volume fractions caused by dissimilar states of preparation, even though they possess the same overall chemical composition (Table 2).

PM HEA exhibited a nano-sized distribution of 89.3 vol% of FCC matrix and 8.0 vol% of evenly dispersed hard TiC particles, in-situ formed during the mechanical milling (Fig. S8), as characterized by TEM in Fig. 4a and EBSD in Fig. 7. These hard particles may have a substantial effect on the tribological properties of the material, as the PM alloy acts as a metal matrix composite, enhancing the wear resistance of the material to some extent. This fact possibly contributes for the enhanced results when subjected to 1.2 N load compared to those of the AISI 52100. This is in accordance with other studies suggesting that some metal-matrix composites may have improved response over traditional wear-resistant steels when subjected to specific conditions [53–56].

Since the wear process under 1.2 N with PM HEA is realized in much

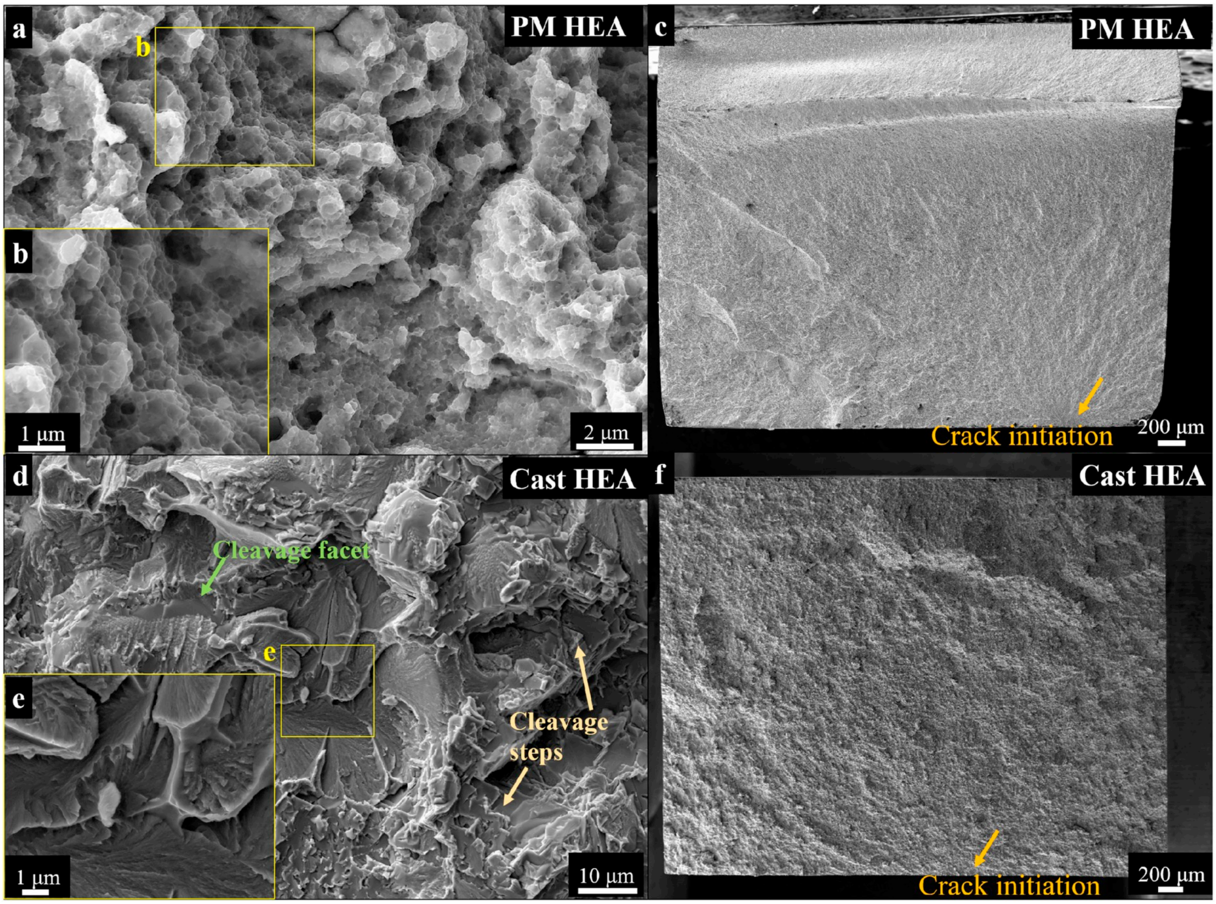

Fig. 9. SEM micrographs of fracture surfaces of $Al_{0.2}Co_{1.5}CrFeNi_{1.5}Ti$ bending specimens. a) Typical PM HEA fracture surface morphology with fine ductile dimples. b) Enlarged view of the area denoted by yellow rectangle showing typical fine ductile dimples. c) PM HEA fracture surface overview with crack initiation site denoted by yellow arrow. d) Typical Cast HEA fracture surface possessing predominantly brittle morphology. Brittle cleavage facets denoted by the green arrow and steps by yellow ones. e) Enlarged view of the area denoted by the yellow rectangle showing typical cleavage separation and river patterns. f) Cast HEA: fracture surface overview. (For interpretation of the references to color in this figure legend, the reader is referred to the web version of this article.)

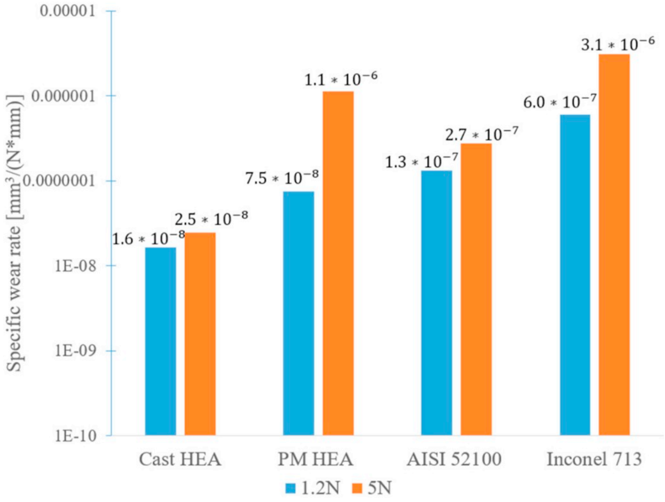

Fig. 10. Specific wear rates of the cast and the PM HEAs in comparison with reference materials (AISI 52100 and Inconel 713) under different load conditions, 1.2 N and 5 N.

smaller contact area as compared to the Cast HEA while the COFs are similar, much higher flash temperature is expected. Higher temperature could further facilitate the formation of adhesive bonds.

Table 4

Total worn volume of each material and corresponding coefficients of friction under 1.2 N and 5 N loads.

Material	Worn volume [µm^3]		COF	
	1.2 N	5 N	1.2 N	5 N
Cast HEA	0.71	1.07	0.67 ± 0.11	0.66 ± 0.04
PM HEA	3.25	48.57	0.74 ± 0.08	0.60 ± 0.04
AISI 52100	5.7	11.85	0.80 ± 0.04	0.67 ± 0.07
Inconel 713	25.96	134.47	0.81 ± 0.05	0.74 ± 0.04

Under higher loads, the tribological performance of the PM alloy decreases. It is assumed that, when the load is increased to 5 N, microcracks are initiated on the very hard TiC particles (revealed in the supplementary material - Fig. S4). They can block the motion of mobile dislocations during shearing, thus, leading to early crack nucleation and propagation and more severe delamination wear. These microcracks essentially lead to inferior results in wear properties at 5 N load.

The combined effect of higher stress intensity (compared to 1.2 N load) and cracking regions leads to wear rate increase in the PM alloy, in agreement with other studies evidencing identical effect upon the same wear conditions for PM alloys [57]. In contrast, there is no evidence of microcracking regions in the Cast HEA even when subjected to high load (as can be observed in Fig. S4 of the supplementary material).

Additionally, since the PM alloy is mostly composed of FCC structure, dislocation slip is facilitated due to lower friction stress compared to, e.g. BCC or other type of structures; i.e. it facilitates the material

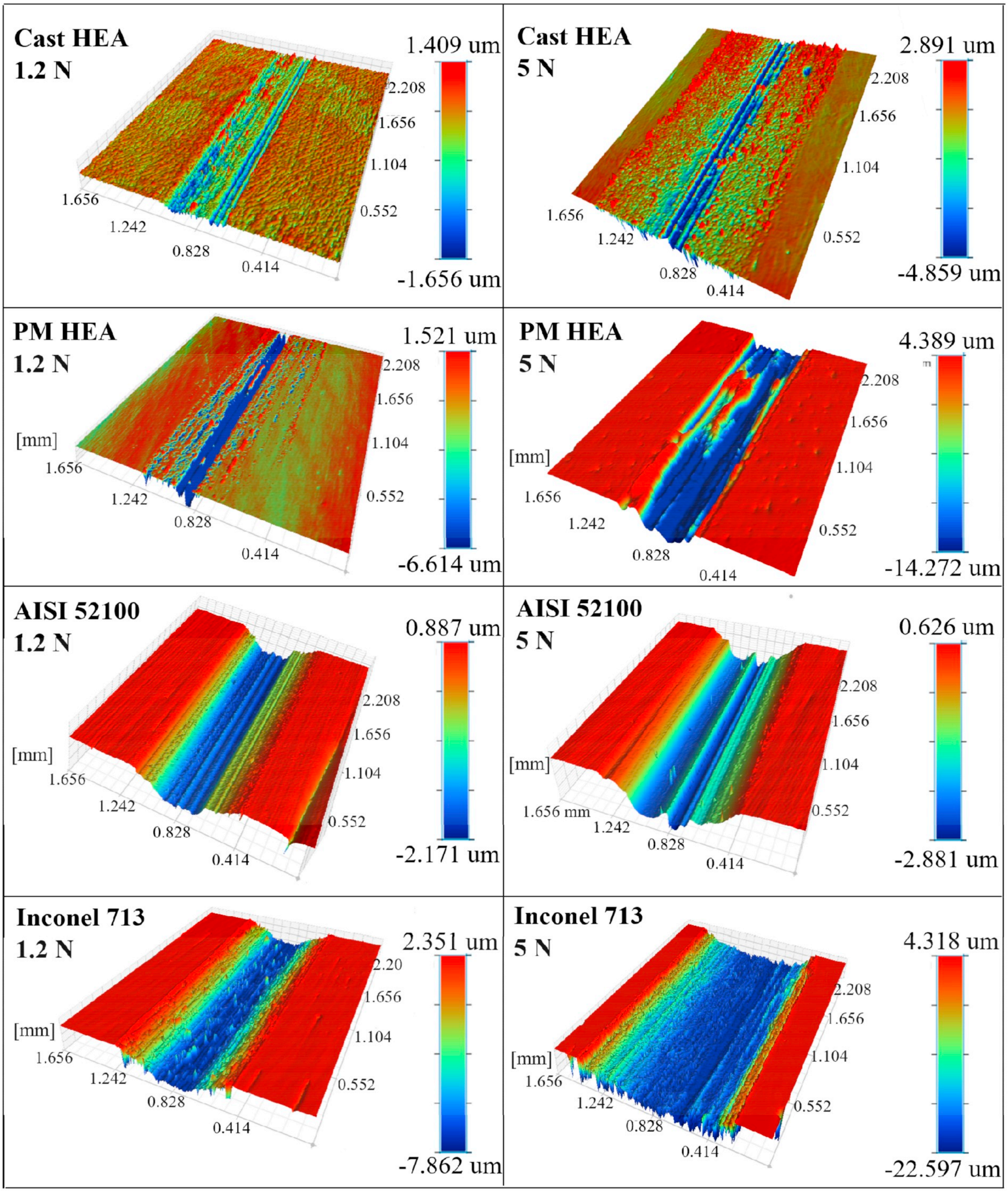

Fig. 11. Three-dimensional wear track profiles of the Cast HEA, PM HEA, AISI 52100 and Inconel 713 formed under 1.2 N and 5 N load forces. Note that the colored scales actually refer to different values in μm (limitation of the software).

deposition in form of adhesive wear [58]. Furthermore, the ductile FCC phase is more susceptible to forming adhesive bonds, i.e. the material with the highest amount of FCC has a stronger tendency to wear at certain conditions.

Both PM and cast alloys are full density samples (99.9% density). Figs. S7 and S8 of the supplementary material reveal the absence of porosity. Therefore, porosity should not be a factor influencing the tribological properties.

Cast HEA exhibits only a negligible amount of non-metallic inclusions typically seen in cast materials. This was characterized by SEM/EDX analysis and shown in Fig. S8. These should not influence the tribological properties of the Cast HEA, as these impurities are not even detected by XRD technique (Fig. 2).

The enhanced wear of the Cast HEA may be especially attributed to the exceptionally hard coarse precipitates of the TCP phases corresponding to a 42.6 vol%, such as Laves phases or, additionally, large mixed areas of Laves, σ, and BCC phases (present in Fig. 8) within the 47.8 vol% of FCC matrix. The material possesses only about half of the volume of the FCC phase compared to PM HEA, therefore reducing the tendency for adhesive wear. Moreover, the coarse brittle phases in the

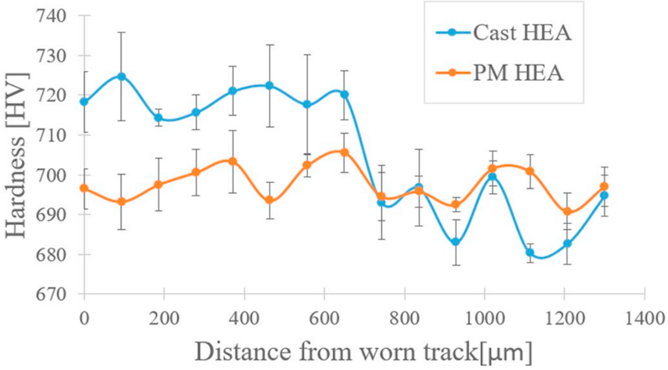

Fig. 12. Plot showing microhardness profiles after wear tests on 5 N load for PM and Cast HEAs. The local hardness under the worn track of Cast HEA increased compared to base material (higher distances) due to local strain hardening. (For interpretation of the references to color in this figure legend, the reader is referred to the web version of this article.)

Cast HEA serve as barriers to delamination wear.

Up to some extent, local strain hardening caused by plastic deformation might play a role on the tribological properties of the Cast HEA, as coarse-grained microstructures have sufficient space for dislocation glide [28]. This is evidenced by the hardness of the Cast HEA worn surface, which increases after the wear test (hardness profiles are exhibited in Fig. 12 for 5 N load). This effect might contribute for the improved wear resistance of the part. In contrast, nanoscale FCC grains present in PM HEA have very limited space for dislocation glide; consequently, no local strain hardening was observed after the wear test, thus exhibiting an inferior performance in comparison with the Cast HEA.

The combination of the aforementioned features leads the Cast HEA to perform exceptionally better than any other under both loading conditions, considering the particular differences between the two states.

As can be seen in Fig. 13, PM HEA possesses an interesting combination of low specific wear rate under 1.2 N load and high flexural strength allied with high hardness. The PM HEA is superior in terms of mechanical bending strength, presenting a strength increase of ~80%, relative to its cast counterpart, while retaining an identical wear rate at 1.2 N. The results of PM HEA's flexural strength are still superior to traditional tool steels such as AISI 52100 [59], AISI A681 O1 [60] and AISI M2 [20,61]. Increasing the load to 5 N during the wear test causes a significant reduction in its wear properties, whereas the Cast HEA wear rate remains relatively unchanged, maintaining its enhanced tribological properties.

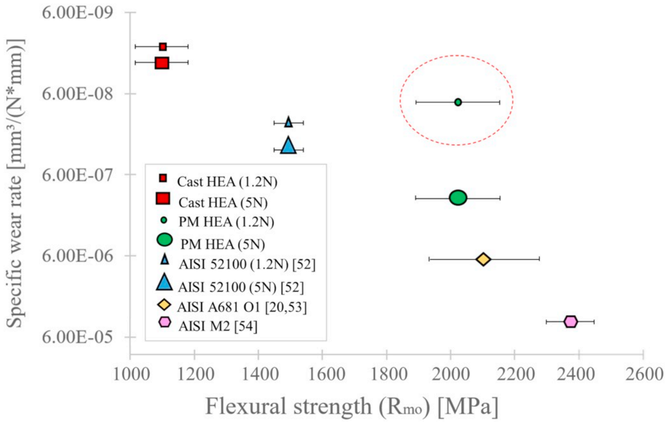

Fig. 13. Specific wear rates vs. flexural strengths (R_{mo}) of both the PM and the Cast HEA in comparison with conventional tool steels. Data for tool steels are taken from [20,59–61].

4. Conclusions

In this study, $Al_{0.2}Co_{1.5}CrFeNi_{1.5}Ti$ high-entropy alloy was produced by two different routes, powder metallurgy (PM) and casting. Owing to differences in the processing, the two alloys differed in a number of qualities, as evaluated through their microstructural features, as well as mechanical and tribological properties. The main outcomes of this investigation can be summarized as follows:

- The manufacturing routes, particularly the processing conditions (such as cold-working by mechanical alloying, temperatures and cooling rates) play an essential role in dictating the final microstructural features, significantly influencing the mechanical and tribological properties of the two alloys.
- The PM route has an inherent tendency to form in-situ carbides during mechanical milling. The main reason is the addition of carbon-based process control agents which are essential for the process. As such, the PM alloy exhibited a uniform, fine-grained microstructure composed almost solely of a nano-sized FCC matrix (89%) with evenly dispersed nano-sized TiC particles (8%, formed in-situ during the mechanical milling), a minor BCC phase and, additionally, intra-granular nano-sized coherent precipitates in an γ/γ' relationship with the matrix. This microstructure is analogous to that of some nickel-based superalloys.
- In contrast, the Cast HEA exhibited a coarse-grained microstructure containing 48% FCC matrix, 10% BCC phase and a 42% mixture of hard intermetallic phases (needle-shaped Laves and σ). Forming the ordered phases is a consequence of the large negative enthalpy, triggering a segregation process during cooling. Both microstructures are in good agreement with the predicted phases obtained by CALPHAD calculation.
- The PM alloy exhibited a remarkable flexural strength R_{mo} = 2018 MPa, elastic modulus E = 258 GPa, and hardness 712 HV. These values were far superior to the cast counterpart (1101 MPa, 210 GPa, 682 HV), which was most likely deteriorated by the high content of unavoidable brittle phases. Surprisingly, in contrast to the strength values, the PM alloy manifested an unexpected ductile fracture behaviour, potentially a consequence of the ductile nature of the FCC phase and a strong TiC particle-matrix interface.
- At low loads, the PM alloy showed wear resistance surpassing that of the conventional wear-resistant tool steel AISI 52100 or Inconel 713. Unfortunately, the wear resistance significantly decreased under an increasing load. Despite the rather weaker mechanical properties, the cast alloy exhibited the best wear properties among all tested materials at both tested loads.
- Mild-oxidational wear is the predominant tribological regime for both PM and Cast HEAs. The adhesive wear tendency of Cast HEA is hindered to some extent, since the volume fraction of the disordered FCC phase is about one-half relative to its PM counterpart, as ductile FCC phase is more inclined to form adhesive bonds. Additionally, the hard TCP phases present in Cast HEA serve as barriers to delamination wear, thus the enhanced wear resistance may be explained.
- In the overall comparison, the PM process is better suited for producing mechanically resistant, fine-grained HEAs with very homogenous microstructures and enhanced wear resistance. On the other hand, casting is better suited for manufacturing wear-resistant HEAs for applications where their intrinsic brittleness is not an issue.

Acknowledgements

This work has been supported by the research project no. 19-22016S of Czech Science Foundation. The project no. FSI-S-17-4711 of Brno

University of Technology is further acknowledged. P.M. acknowledges financial support by ERDF under project No. CZ.02.1.01/0.0/0.0/15 003/0000485. The authors would like to gratefully acknowledge the contributions of Ing. Zdenek Spotz, Ph.D. for the XRD analyses and Ing. Josef Zapletal, Ph.D. for the bending experiments.

Data availability

The processed data required to reproduce these findings are available by e-mail to the corresponding author: gouvea@fme.vutbr.cz.

Declaration of competing interest

The authors declare that they have no conflict of interest.

Appendix A. Supplementary data

Supplementary data to this article can be found online at https://doi.org/10.1016/j.matchar.2019.110046.

References

[1] Y. Zhang, T.T. Zuo, Z. Tang, M.C. Gao, K.A. Dahmen, P.K. Liaw, Z.P. Lu, Microstructures and properties of high-entropy alloys, Prog. Mater. Sci. 61 (2014) 1–93, https://doi.org/10.1016/j.pmatsci.2013.10.001.
[2] D.B. Miracle, J.D. Miller, O.N. Senkov, C. Woodward, M.D. Uchic, J. Tiley, Exploration and development of high entropy alloys for structural applications, Entropy. 16 (2014) 494–525, https://doi.org/10.3390/e16010494.
[3] Y.F. Ye, Q. Wang, J. Lu, C.T. Liu, Y. Yang, High-entropy alloy: challenges and prospects, Mater. Today 19 (2016) 349–362, https://doi.org/10.1016/j.mattod.2015.11.026.
[4] J.-W. Yeh, S.-K. Chen, S.-J. Lin, J.-Y. Gan, T.-S. Chin, T.-T. Shun, C.-H. Tsau, S.-Y. Chang, Nanostructured high-entropy alloys with multiple principal elements: novel alloy design concepts and outcomes, Adv. Eng. Mater. 6 (2004) 299–303, https://doi.org/10.1002/adem.200300567.
[5] J.-W. Yeh, Physical metallurgy of high-entropy alloys, JOM. 67 (2015) 2254–2261, https://doi.org/10.1007/s11837-015-1583-5.
[6] B.S. Murty, J.W. Yeh, S. Ranganathan, B.S. Murty, J.W. Yeh, S.B.T.-H.E.A., Ranganathan (Eds.), Chapter 2 - High-Entropy Alloys: Basic Concepts, Butterworth-Heinemann, Boston, 2014, pp. 13–35, , https://doi.org/10.1016/B978-0-12-800251-3.00002-X.
[7] Y. Dong, Y. Lu, L. Jiang, T. Wang, T. Li, Effects of electro-negativity on the stability of topologically close-packed phase in high entropy alloys, Intermetallics. 52 (2014) 105–109, https://doi.org/10.1016/j.intermet.2014.04.001.
[8] X. Yang, Y. Zhang, Prediction of high-entropy stabilized solid-solution in multi-component alloys, Mater. Chem. Phys. 132 (2012) 233–238, https://doi.org/10.1016/j.matchemphys.2011.11.021.
[9] C.-J. Tong, Y.-L. Chen, J.-W. Yeh, S.-J. Lin, S.-K. Chen, T.-T. Shun, C.-H. Tsau, S.-Y. Chang, Microstructure characterization of AlxCoCrCuFeNi high-entropy alloy system with multiprincipal elements, Metall. Mater. Trans. A 36 (2005) 881–893, https://doi.org/10.1007/s11661-005-0283-0.
[10] O.N. Senkov, S.V. Senkova, C. Woodward, Effect of aluminum on the microstructure and properties of two refractory high-entropy alloys, Acta Mater. 68 (2014) 214–228, https://doi.org/10.1016/j.actamat.2014.01.029.
[11] K. Zhang, Z. Fu, Effects of annealing treatment on phase composition and microstructure of CoCrFeNiTiAlx high-entropy alloys, Intermetallics. 22 (2012) 24–32, https://doi.org/10.1016/j.intermet.2011.10.010.
[12] Y. Zhang, Y.J. Zhou, J.P. Lin, G.L. Chen, P.K. Liaw, Solid-solution phase formation rules for multi-component alloys, Adv. Eng. Mater. 10 (2008) 534–538, https://doi.org/10.1002/adem.200700240.
[13] Z. Li, K.G. Pradeep, Y. Deng, D. Raabe, C.C. Tasan, Metastable high-entropy dual-phase alloys overcome the strength–ductility trade-off, Nature. 534 (2016) 227, https://doi.org/10.1038/nature17981.
[14] D. Raabe, C.C. Tasan, H. Springer, M. Bausch, From high-entropy alloys to high-entropy steels, Steel Res. Int. 86 (2015) 1127–1138, https://doi.org/10.1002/srin.201500133.
[15] I. Moravcik, J. Cizek, J. Zapletal, Z. Kovacova, J. Vesely, P. Minarik, M. Kitzmantel, E. Neubauer, I. Dlouhy, Microstructure and mechanical properties of Ni1,5Co1,5CrFeTi0,5 high entropy alloy fabricated by mechanical alloying and spark plasma sintering, Mater. Des. 119 (2017) 141–150, https://doi.org/10.1016/j.matdes.2017.01.036.
[16] S.S. Nene, M. Frank, K. Liu, S. Sinha, R.S. Mishra, B. McWilliams, K.C. Cho, Reversed strength-ductility relationship in microstructurally flexible high entropy alloy, Scr. Mater. 154 (2018) 163–167, https://doi.org/10.1016/j.scriptamat.2018.05.043.
[17] B. Gludovatz, A. Hohenwarter, D. Catoor, E.H. Chang, E.P. George, R.O. Ritchie, A fracture-resistant high-entropy alloy for cryogenic applications, Science 345 (2014) 1153 LP–1158, https://doi.org/10.1126/science.1254581 (80-.).
[18] H.M. Daoud, A.M. Manzoni, N. Wanderka, U. Glatzel, High-temperature tensile strength of Al10Co25Cr8Fe15Ni36Ti6 compositionally complex alloy (high-entropy alloy), JOM. 67 (2015) 2271–2277, https://doi.org/10.1007/s11837-015-1484-7.
[19] S. Praveen, H.S. Kim, High-entropy alloys: potential candidates for high-temperature applications – an overview, Adv. Eng. Mater. 20 (2018) 1700645, , https://doi.org/10.1002/adem.201700645.
[20] M.-H. Chuang, M.-H. Tsai, W.-R. Wang, S.-J. Lin, J.-W. Yeh, Microstructure and wear behavior of AlxCo1.5CrFeNi1.5Tiy high-entropy alloys, Acta Mater. 59 (2011) 6308–6317, https://doi.org/10.1016/j.actamat.2011.06.041.
[21] Y.Y. Zhao, H.W. Chen, Z.P. Lu, T.G. Nieh, Thermal stability and coarsening of coherent particles in a precipitation-hardened (NiCoFeCr)94Ti2Al4 high-entropy alloy, Acta Mater. 147 (2018) 184–194, https://doi.org/10.1016/j.actamat.2018.01.049.
[22] M.J. Yao, K.G. Pradeep, C.C. Tasan, D. Raabe, A novel, single phase, non-equiatomic FeMnNiCoCr high-entropy alloy with exceptional phase stability and tensile ductility, Scr. Mater. 72–73 (2014) 5–8, https://doi.org/10.1016/j.scriptamat.2013.09.030.
[23] Y. Shi, B. Yang, K.P. Liaw, Corrosion-resistant high-entropy alloys: a review, Met. 7 (2017), https://doi.org/10.3390/met7020043.
[24] M. Löbel, T. Lindner, T. Lampke, Enhanced wear behaviour of spark plasma sintered AlCoCrFeNiTi high-entropy alloy composites, Mater. (Basel, Switzerland). 11 (2018) 2225, https://doi.org/10.3390/ma11112225.
[25] O.N. Senkov, G.B. Wilks, D.B. Miracle, C.P. Chuang, P.K. Liaw, Refractory high-entropy alloys, Intermetallics. 18 (2010) 1758–1765, https://doi.org/10.1016/j.intermet.2010.05.014.
[26] I. Moravcik, L. Gouvea, V. Hornik, Z. Kovacova, M. Kitzmantel, E. Neubauer, I. Dlouhy, Synergic strengthening by oxide and coherent precipitate dispersions in high-entropy alloy prepared by powder metallurgy, Scr. Mater. 157 (2018), https://doi.org/10.1016/j.scriptamat.2018.07.034.
[27] I. Moravcik, L. Gouvea, J. Cupera, I. Dlouhy, Preparation and properties of medium entropy CoCrNi/boride metal matrix composite, J. Alloys Compd. 748 (2018), https://doi.org/10.1016/j.jallcom.2018.03.204.
[28] Z. Fu, W. Chen, H. Wen, D. Zhang, Z. Chen, B. Zheng, Y. Zhou, E.J. Lavernia, Microstructure and strengthening mechanisms in an FCC structured single-phase nanocrystalline Co25Ni25Fe25Al7.5Cu17.5 high-entropy alloy, Acta Mater. 107 (2016) 59–71, https://doi.org/10.1016/j.actamat.2016.01.050.
[29] I. Moravcik, J. Cizek, L. Gouvea, J. Cupera, I. Guban, I. Dlouhy, Nitrogen interstitial alloying of CoCrFeMnNi high entropy alloy through reactive powder milling, Entropy. 21 (2019) 363, https://doi.org/10.3390/e21040363.
[30] W.C. Oliver, G.M. Pharr, An improved technique for determining hardness and elastic modulus using load and displacement sensing indentation experiments, J. Mater. Res. 7 (1992) 1564–1583, https://doi.org/10.1557/JMR.1992.1564.
[31] J.F. Archard, Contact and rubbing of flat surfaces, J. Appl. Phys. 24 (1953) 981–988, https://doi.org/10.1063/1.1721448.
[32] A. Renger, K.L. Johnson, Contact Mechanics. Cambridge etc., Cambridge University Press 1985. XII, 452 pp., £ 17.50 P/B. ISBN 0521347963, ZAMM - J. Appl. Math. Mech./Zeitschrift Für Angew. Math. Und Mech 69 (1989) 214, https://doi.org/10.1002/zamm.19890690713.
[33] X.D. Xu, S. Guo, T.G. Nieh, C.T. Liu, A. Hirata, M.W. Chen, Effects of mixing enthalpy and cooling rate on phase formation of AlxCoCrCuFeNi high-entropy alloys, Materialia. 6 (2019) 100292, , https://doi.org/10.1016/j.mtla.2019.100292.
[34] M.J. Donachie, S.J. Donachie, Superalloys: A Technical Guide, 2nd edition, (2002).
[35] K.A. Christofidou, T.P. McAuliffe, P.M. Mignanelli, H.J. Stone, N.G. Jones, On the prediction and the formation of the sigma phase in CrMnCoFeNix high entropy alloys, J. Alloys Compd. 770 (2019) 285–293, https://doi.org/10.1016/j.jallcom.2018.08.032.
[36] N. Saunders, A.P.B.T.-P.M.S., Miodownik (Eds.), Chapter 4 - Experimental Determination of Thermodynamic Quantities and Phase Diagrams, CALPHAD Calc. Phase Diagrams, Pergamon, 1998, pp. 61–87, , https://doi.org/10.1016/S1470-1804(98)80024-2.
[37] E.J. Pickering, R. Muñoz-Moreno, H.J. Stone, N.G. Jones, Precipitation in the equiatomic high-entropy alloy CrMnFeCoNi, Scr. Mater. 113 (2016) 106–109, https://doi.org/10.1016/j.scriptamat.2015.10.025.
[38] I. Moravcik, J. Cizek, P. Gavendova, S. Sheikh, S. Guo, I. Dlouhy, Effect of heat treatment on microstructure and mechanical properties of spark plasma sintered AlCoCrFeNiTi0.5 high entropy alloy, Mater. Lett. 174 (2016) 53–56, https://doi.org/10.1016/j.matlet.2016.03.077.
[39] P. Huang, G.Q. Dai, F. Wang, K.W. Xu, Y.H. Li, Fivefold annealing twin in nanocrystalline Cu, Appl. Phys. Lett. 95 (2009) 203101, , https://doi.org/10.1063/1.3263948.
[40] Y. Li, L. Wan, K. Chen, A look-up table based approach to characterize crystal twinning for synchrotron X-ray Laue microdiffraction scans, J. Appl. Crystallogr. 48 (2015) 747–757, https://doi.org/10.1107/S1600576715004896.
[41] B.C. De Cooman, Y. Estrin, S.K. Kim, Twinning-induced plasticity (TWIP) steels, Acta Mater. 142 (2018) 283–362, https://doi.org/10.1016/j.actamat.2017.06.046.
[42] T. Baudin, A.L. Etter, R. Penelle, Annealing twin formation and recrystallization study of cold-drawn copper wires from EBSD measurements, Mater. Charact. 58 (2007) 947–952, https://doi.org/10.1016/j.matchar.2006.09.009.
[43] Y.-J. Chang, A.-C. Yeh, The evolution of microstructures and high temperature properties of AlxCo1.5CrFeNi1.5Tiy high entropy alloys, J. Alloys Compd. 653 (2015) 379–385, https://doi.org/10.1016/j.jallcom.2015.09.042.
[44] R.O. Elliott, C.P. Kempter, Thermal expansion of some transition metal carbides, J. Phys. Chem. 62 (1958) 630–631, https://doi.org/10.1021/j150563a030.
[45] B.S. Murty, J.W. Yeh, S. Ranganathan, B.S. Murty, J.W. Yeh, S.B.T.-H.E.A., Ranganathan (Eds.), Chapter 7 - Intermetallics, Interstitial Compounds and Metallic Glasses in High-Entropy Alloys, Butterworth-Heinemann, Boston, 2014, pp. 119–131, , https://doi.org/10.1016/B978-0-12-800251-3.00007-9.

[46] R. Chang, L.J. Graham, Low-temperature elastic properties of ZrC and TiC, J. Appl. Phys. 37 (1966) 3778–3783, https://doi.org/10.1063/1.1707923.

[47] T.L. Anderson, Fracture Mechanics, 4th ed., CRC Press, Boca Raton, 2017, https://doi.org/10.1201/9781315370293.

[48] S.W. Freiman, J. Mecholsky, The Fracture of Brittle Materials: Testing and Analysis, (2012), https://doi.org/10.1002/9781118147757.

[49] D. Hull, D.J. Bacon, D. Hull, D.J.B.T.-I. to D, Fifth E. Bacon (Eds.), Chapter 3 - Movement of Dislocations, Butterworth-Heinemann, Oxford, 2011, pp. 43–62, , https://doi.org/10.1016/B978-0-08-096672-4.00003-7.

[50] D. Hull, D.J. Bacon, D. Hull, D.J.B.T.-I. to D, Fifth E. Bacon (Eds.), Chapter 10 - Strength of Crystalline Solids, Butterworth-Heinemann, Oxford, 2011, pp. 205–249, , https://doi.org/10.1016/B978-0-08-096672-4.00010-4.

[51] S.C. Lim, M.F. Ashby, Overview no. 55 wear-mechanism maps, Acta Metall. 35 (1987) 1–24, https://doi.org/10.1016/0001-6160(87)90209-4.

[52] Y. Wang, T. Lei, J. Liu, Tribo-metallographic behavior of high carbon steels in dry sliding: I. Wear mechanisms and their transition, Wear. 231 (1999) 1–11, https://doi.org/10.1016/S0043-1648(99)00115-5.

[53] P. Ravindran, K. Manisekar, P. Rathika, P. Narayanasamy, Tribological properties of powder metallurgy – processed aluminium self lubricating hybrid composites with SiC additions, Mater. Des. 45 (2013) 561–570, https://doi.org/10.1016/j.matdes.2012.09.015.

[54] S. Mahdavi, F. Akhlaghi, Effect of the SiC particle size on the dry sliding wear behavior of SiC and SiC-Gr-reinforced Al6061 composites, J. Mater. Sci. 46 (2011) 7883–7894, https://doi.org/10.1007/s10853-011-5776-1.

[55] V. Matějka, Y. Lu, L. Jiao, L. Huang, G. Simha Martynková, V. Tomášek, Effects of silicon carbide particle sizes on friction-wear properties of friction composites designed for car brake lining applications, Tribol. Int. 43 (2010) 144–151, https://doi.org/10.1016/j.triboint.2009.05.007.

[56] E.R.I. Mahmoud, M. Takahashi, T. Shibayanagi, K. Ikeuchi, Wear characteristics of surface-hybrid-MMCs layer fabricated on aluminum plate by friction stir processing, Wear. 268 (2010) 1111–1121, https://doi.org/10.1016/j.wear.2010.01.005.

[57] Z. Sinha, A. Farhat, Effect of surface porosity on tribological properties of sintered pure Al and Al 6061, Mater. Sci. Appl. 6 (2015) 549–566, https://doi.org/10.4236/msa.2015.66059.

[58] J.-M. Wu, S.-J. Lin, J.-W. Yeh, S.-K. Chen, Y.-S. Huang, H.-C. Chen, Adhesive wear behavior of AlxCoCrCuFeNi high-entropy alloys as a function of aluminum content, Wear. 261 (2006) 513–519, https://doi.org/10.1016/j.wear.2005.12.008.

[59] A.D. Anoop, A.S. Sekhar, M. Kamaraj, K. Gopinath, Modelling the mechanical behaviour of heat-treated AISI 52100 bearing steel with retained austenite, Proc. Inst. Mech. Eng. Part L J. Mater. Des. Appl. 232 (2015) 44–57, https://doi.org/10.1177/1464420715612235.

[60] L. Hitachi Metals, General Catalog of YSS Tool Steels, https://www.hitachi-metals.co.jp/e/products/auto/ml/pdf/yss_tool_steels_d.pdf, (2015) , Accessed date: 5 August 2019.

[61] G. Design, Tool steel, molybdenum alloy, AISI M2, regular carbon (high speed), CES EDUPACK. (2017) 1–5 https://riunet.upv.es/bitstream/handle/10251/113733/ANEXO_15329653939736146149195128546168.pdf?sequence=2&isAllowed=y , Accessed date: 3 August 2019.